Article

Cobalt-Free Layered LiNi$_{0.8}$Mn$_{0.15}$Al$_{0.05}$O$_2$/Graphene Aerogel Composite Electrode for Next-Generation Li-Ion Batteries

Deniz Kuruahmet,* Aslihan Guler, Sidika Yildirim, Mustafa Mahmut Singil, Hatice Güngör, Esma Uzun, Engin Alkan, Mehmet Oguz Guler, and Hatem Akbulut

Read Online

ACCESS | Metrics & More | Article Recommendations

ABSTRACT: In this work, we introduce LiNi$_{0.8}$Mn$_{0.15}$Al$_{0.05}$O$_2$ (NMA), which is cobalt-free and has a high nickel content, and a conductive composite material to NMA by supporting it with a three-dimensional (3D) graphene aerogel (GA). With an easy freeze-drying approach, NMA nanoparticles are properly dispersed on graphene sheets, and GA creates a strong and conductive framework, significantly improving the structure and conductivity. The structure of the pure NMA and NMA/graphene aerogel (NMA/GA) composite was investigated by X-ray diffraction (XRD) and field emission scanning electron microscopy (FE-SEM). XRD and FE-SEM analyses clearly indicated that ultrapure NMA structures are homogeneously dispersed among the GAs. In addition, the composite structure was examined using transmission electron microscopy (TEM) to determine the dispersion mechanisms. The electrochemical cycling performance of the pure NMA and NMA/GA composite was evaluated by rate capacitance, cyclic voltammetry (CV), and electrochemical impedance spectroscopy (EIS). The synthesized NMA/GA was able to provide 89.81% specific capacity retention after the 500th cycle at C/2. The average charge/discharge rates of the obtained cathode show good electrochemical results and exhibit capacities of 190.2, 186.3, 185.2, 176.2, 161.2, 142.6, and 188.5 mAh g^{-1} at C/20, C/10, C/5, C, 3C, 5C, and C/20, respectively. EIS data showed an improvement in the impedance of the composite containing GA. According to the results of the electrochemical tests, NMA nanoparticles formed a conductive network with its porous structure thanks to GA, formed a protective layer on the surface, prevented the side reactions between the cathode and the electrolyte, decreased the impedance of the cathode, and increased the redox kinetics. In addition, the changes in the structure were investigated in the NMA/GA composite cathode by XRD, FE-SEM, and Raman analyses at the end of the 50th, 250th, and 500th cycles. In summary, the NMA/GA cathode is expected to play an important role in lithium-ion batteries (LIBs) by taking advantage of its easy synthesis and excellent cycle stability.
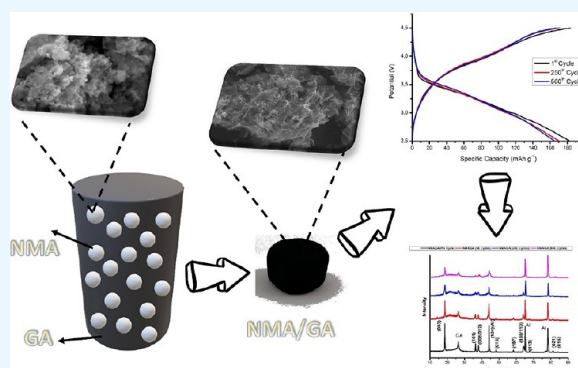
INTRODUCTION

LIBs have beneficial properties such as high storage capacity, enhanced performance life, excellent rate capability, and eco-friendliness. Applications of LIBs in plug-in electric vehicles, hybrid electric vehicles, and electric vehicles (EVs) have been limited because of the low capacity of positive electrodes such as LiMn$_2$O$_4$, LiCoO$_2$, and LiFePO$_4$. For this reason, it is necessary to produce new cathodes with high energy density and specific capacity.[1−14]

Recently, LiNi$_{1−x−y}$Co$_x$Al$_y$O$_2$ (NCA) and Li-Ni$_{1−x−y}$Mn$_x$Co$_y$O$_2$ (NMC) layered metal oxides have attracted more attention than conventional LiCoO$_2$ due to their improved structural stability and electrochemical properties. Cathodes with high Ni contents are the preferred materials for new-generation high-energy lithium-ion batteries.[15,16] This new generation of layered oxides with high nickel contents contributes to the extraordinary growth of the electric vehicle

market as they reach energy densities of approximately 650 Wh kg^{-1}.[17] The crystal structures of NCA and NMC have layered phases similar to the LiNiO$_2$ rhombohedral phase (R-3m) with Ni ion substitution.[18] Ni^{2+}, which is found together with Ni^{3+} during the calcination process, occupies the 3b regions with their ionic radius of 0.69 Å, as they are close to the radius of Li ions (0.76 Å).[19,20] Cobalt in NMC and NCA cathodes is extracted as a byproduct in copper or nickel mines. For these reasons, cobalt is known as an expensive and rare metal.[21] Figure 1 shows the price fluctuations of cobalt on the London
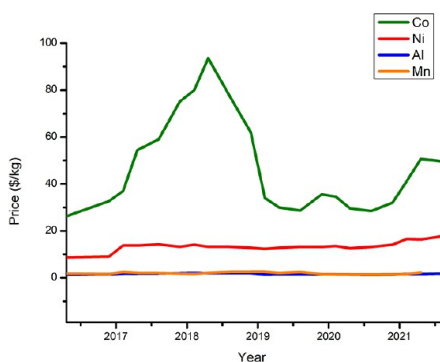
Figure 1. The market price of cobalt, nickel, manganese, and aluminum.

Metal Exchange since 2016.[22−25] Existing research is trying to further reduce production costs by eliminating cobalt dependence in cathode materials.[26] Tesla announced that it will develop and use cathodes with a cobalt content of less than 3% for LIBs used in EVs. Cobalt-free cathodes have been seen as an alternative to commercial Ni-layered oxide cathode materials, but there are still challenges in their practical application. The terms "Co-free" and "Ni-rich" refer to a return to the $LiNiO_2$ family, which was researched many years ago and cannot be used commercially because of the many problems with its natural stoichiometry.[27] Low-Ni-content cathodes have lower energy compared to Ni-rich cathode materials such as NMC and NCA due to their low Coulomb efficiencies,[28] Ni^{3+} instability,[29] Li^+/Ni^{2+} cation mixing,[30] and thermal instability.[31] Because of these disadvantages, Co-free high Ni-layered oxides such as Mn^{4+} and Al^{3+}, which are stable and have a high specific capacity with suitable doping, should be developed.[32,33]

Here, a new nickel-rich Li-ion battery cathode material with the general formula $LiNi_xMn_yAl_zO_2$ ($x \geq 0.8$, $x + y + z = 1$) belonging to the NMA layered cathode class is presented. The NMA crystal structure, which has a layered structure, is similar to NMC and NCA, with $O^{2−}$ ions in the 6c site, Li^+ in the 3a site, and transition metal (TM) (Ni, Mn, Al) ions in the 3b site (Figure 2).[34] These new cobalt-free NMA cathodes reduce
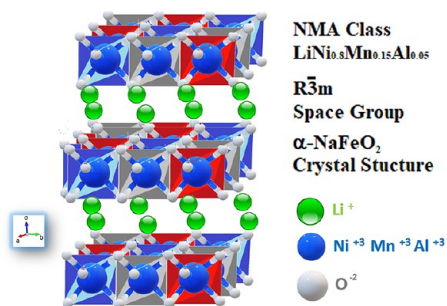

Figure 2. Schematic representation of the NMA crystal structure.

cost and increase capacity (≈200 mAh g^{-1}) while retaining the structural stability and safety advantages afforded by manganese and aluminum and the high capacity offered by nickel.

It has been shown that Mn^{4+} in the structure is effective in improving thermal stability as it suppresses the large exothermic reaction. However, the Mn element cannot reduce the cationic mixture of Li^+ and Ni^{2+} because of the magnetic dipole−dipole interaction in the TM layer. To reduce this mixing, the Al^{3+} element with unpaired electrons is needed as an alternative to Co, which prevents cation mixing.[32] In the study by Zheng et al.,[35] it was mentioned that the enthalpy of the formation of Al is higher than that of Ni. It shows that Al enhances structural stability, minimizes harmful phase transition, can be used to optimize thermal and electrochemical properties, and thus is sufficient to improve thermal stability even without Co in the structure. The strong covalent Al−O bond prevents the moisture/carbon dioxide-induced reaction on the oxide surface.[36] In addition, 33−50 mol % Mn can be added to Ni-based layered oxides,[37] and the use of Al is generally limited to ≤5−6% mol % to avoid secondary phases.[38]

However, NMA cathodes with high nickel contents have poor electrical conductivity, which degrades the performance of batteries. Therefore, to improve the performance of the battery, a carbon matrix supplement can play a supporting role in increasing conductivity.

Graphene, one of the 2D carbonaceous materials, is seen as an ideal electrode additive material due to its unique mechanical properties and enhanced electrochemical performances. The functional groups on graphene sheets act as radical centers to store Li ions at high potential. Graphene composite cathodes have porous morphology and high electrical conductivity. The well-connected developed pores in the graphene cathodes and the C=O functional groups evenly distributed in the material act as a redox center for the storage of Li ions. By partial reduction of graphite oxide, the appropriate amount of C=O bonds to be used in the cathode material is expected to increase the electrical conductivity while maintaining the redox center.[39,40] However, the graphene sheets exhibit much lower electrochemical performance than expected, as they are restacked into a graphite-like structure during the preparation/storage process. One solution to overcome this is to transform two-dimensional graphene sheets into a 3D structure.[41] GA-based composites can be formed as a result of the 3D structure and large surface area provided by GA, providing more active sites and fast electron transport kinetics.[42−45] The interlocking 3D macropores of GA can improve the transport pathway of Li^+ ions, allowing better penetration of the electrolyte and thereby increasing the electrode capacity and significantly accelerating the electron transfer necessary to further increase the rated capacity of lithium-ion batteries.[46] Tian et al.[47] developed a new 3D porous graphene aerogel composite to increase the contact area of the $LiNi_{0.6}Co_{0.2}Mn_{0.2}O_2$ nanoparticle with the cathode and electrolyte and showed superior electrochemical properties compared to pure $LiNi_{0.6}Co_{0.2}Mn_{0.2}O_2$.

Herein, we report for the first time NMA nanoparticles were synthesized by the sol−gel method. GA used to construct a novel 3D porous stucture wrapped with NMA nanoparticle was synthesized via reduction of graphene oxide (GO). A modified Hummers technique was applied to prepare GO using graphite powder. Ascorbic acid was used as the reducing agent to prepare the graphene hydrogel. A rational design and fabrication of lightweight 3D hierarchical porous NMA/GA composites with a 3D porous network architecture were investigated. A 3D conductive GA-reinforcing NMA composite was successfully prepared. Our electrochemical tests clearly demonstrated that the unique 3D architecture from the produced NMA/GA results in tremendous battery performance at up to 500 cycles.

EXPERIMENTAL PROCEDURE

Synthesis of NMA Nanoparticles. NMA nanoparticles used as active materials were synthesized via the sol−gel method (Figure 3). In this process, 1.02 g of $LiCH_3COO_2\cdot$
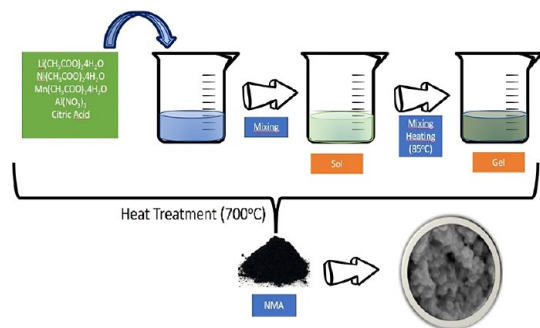

Figure 3. Synthesis of NMA nanoparticles by the sol−gel method.

H_2O, 1.99 g of $Ni(CH_3COO)_2\cdot4H_2O$, 0.367 g of Mn-$(CH_3COO)_2\cdot4H_2O$, and 0.187 g of $Al(NO_3)_3\cdot H_2O$ were dissolved in 100 mL of distilled water followed by the addition of 1 mmol of citric acid as complexing agent into the solution. The solution was unceasingly stirred at 85 °C until a transparent semifluid gel was obtained. The obtained gel was dried in an oven for 24 h at 60 °C. The product was calcined at 700 °C for 8 h in the furnace.

Preparation of the NMA/GA Composite. The modified Hummers method was used in the synthesis of GO produced from natural flake graphite. Ultrasonication was used to prepare the GO aqueous suspension with 3.0 mg mL^{-1} of GO (30 wt %). L-Ascorbic acid (L-AA, 180 mg) was dispersed into 20 mL of GO solution and sonicated for 30 min. Then, 140 mg of prepared NMA (70 wt %) nanoparticles was added into GO solutions and sonicated for another 30 min. Then, the mixture was subjected to heating at 65 °C for 8 h with no stirring to get the graphene hydrogel (Figure 4). After naturally cooling, the
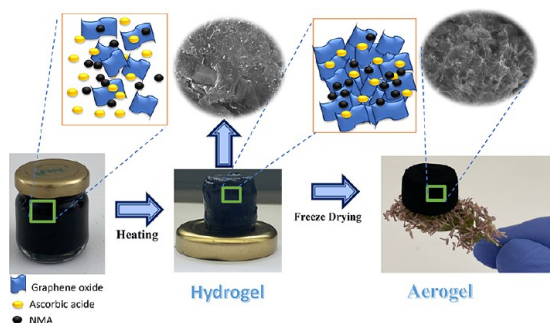

Figure 4. Synthesis of the NMA/GA composite.

cylinder formed spontaneously and was then washed with distilled water to remove excess L-AA. The hydrogel was then freeze-dried to obtain GA. Finally, it was freeze-dried to form 3D porous NMA/GA.

Cell Preparation. Pure NMA and NMA/GA cathodes were prepared by the classical slurry preparation method. Polyvinylidene fluoride binder (10 wt %) in 4 mL of *N*-methyl-2-pyrrolidinone solution, 10 wt %. conductive additive, and 80 wt %. active materials were stirred for 2 h to form a homogeneous slurry. The prepared slurry was uniformly

coated onto the aluminum foil using a doctor blade and dried overnight at 65 °C for 12 h in a vacuum oven.

Material Characterizations. The characterizations of the crystalline structures of pure NMA and NMA/GA cathodes were carried out using the Rigaku DMax 2200 XRD within the range of 10−80°. FE-SEM (FEI Quanta Q400) and energy-dispersive X-ray spectroscopy (EDS) were used to investigate the morphologies and chemical composition of the samples. TEM images were taken using a Tecnai T20 microscope with a 200 kV electron source. The specific surface area and pore size distribution were identified by nitrogen adsorption/desorption measurement. Fourier transform infrared spectra (FTIR) were recorded on an FTIR spectrometer. The thermal behavior of the produced composites was evaluated by thermal gravimetric analysis (TGA) with the Netzsch STA 441 Jupiter in the range of 30−900 °C at a heating rate of 5 °C min^{-1} in the air atmosphere. X-ray photoelectron spectroscopy (XPS, Thermo Scientific K-Alpha) was used to identify the chemical compositions and surface electron structure of the samples. The specific surface area was calculated by the multipoint Brunauer−Emmett−Teller (BET) method.

Electrochemical Analysis. Electrochemical performance tests of pure NMA and NMA/GA cathodes were performed in a half-cell configuration using a button cell battery (CR2032) with Li metal as the counter electrode. The test cell was collected in a glove box under an Ar atmosphere using polypropylene (pp) as the separator and 1 M $LiPF_6$ as the electrolyte. The electrochemical performance of NMA and NMA/GA electrodes was analyzed at room temperature (25 °C) using a computer-controlled battery tester between 2.5 and 4.5 V at C/2 rate.

RESULTS AND DISCUSSION

Physical Characterization, Surface Morphology, and Composition of NMA and NMA/GA Cathodes. According
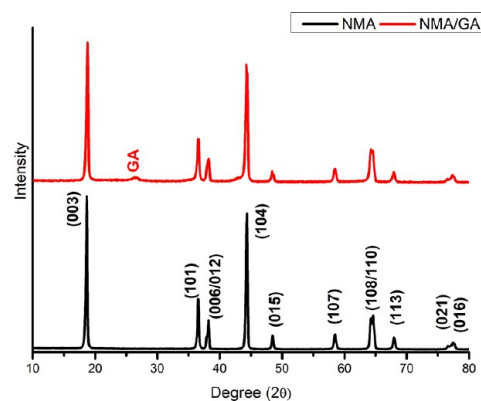

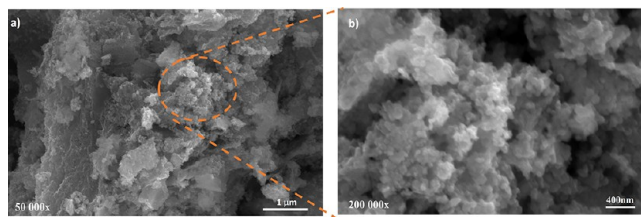**Figure 5.** XRD patterns of the NMA and NMA/GA.

Figure 6. FE-SEM images of NMA nanoparticles: (a) 50,000× and (b) 200,000×.
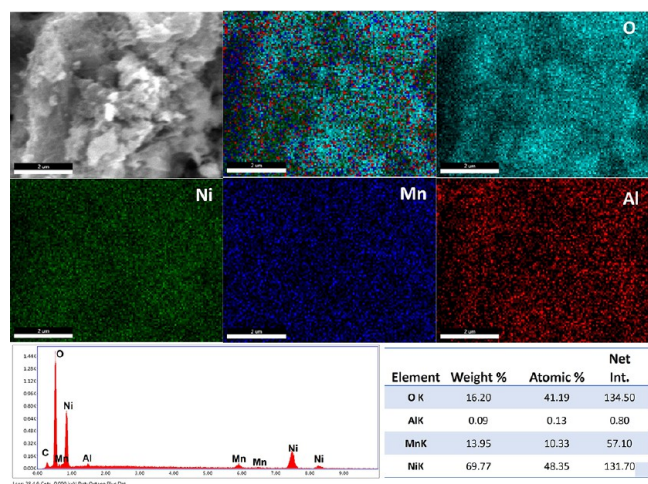
Figure 7. EDS dot-mapping images and EDS analysis of NMA.

to the XRD patterns shown in Figure 5, the NMA peaks are indexed as layered oxide based on the highly sharp and well-defined α-NaFeO$_2$-type hexagonal structure (space group R-$3m$, JPDS Card No. 070-4312). No impurity could be detected in the prepared sample. Li sites are partially engaged by Ni ions that have similar ionic radii (Ni^{2+} 0.69 Å and Li$^+$ 0.76 Å). The intensity ratio $I_{(003)}/I_{(104)}$, which is calculated based on the intensity value that is the area under the corresponding peak, gives information about the degree of cation mixing of Li$^+$/Ni^{2+} (partial Ni^{2+} ion occupation on Li$^+$ sites) and the measure of the electrochemical reactivity of the cathode material.[48] As shown in literature publications, the Li$^+$/Ni^{2+} mixing degree is defined as "acceptable" when the cation mixture value (003)/(104) is >1.2. The cation mixing ratio of the produced NMA nanoparticles was calculated as 1.25.[49] The ratio $I_{(003)}/I_{(104)}$ of the NMA particles produced by the sol−gel method is above the limit value, expressly showing that there is no cation mixture in the structure. The lattice parameters of NMA nanoparticles were calculated, and a = 2.8824 Å and c = 14.2395 Å values were obtained. The ratio of the c parameter and a parameter (c/a) is defined as lattice distortion, and the c/a value was found to be 4.94. The peaks (006/012) and

(108/110) in all samples were clearly defined at 2θ = 38 and 65°, respectively, indicating that the NMA nanoparticles had a layered structure. NMA and NMA/GA hybrid cathode materials have both high purity and strong layered structure. The Scherrer equation is used to determine the size of crystal particles.[50]

$$D = \frac{k\lambda}{\beta_{\text{hkl}}\cos\theta}$$

In the above equation, D is the crystal size, λ is the X-ray wavelength, k is the shape factor (k = 0.9), β is the full width at the half maximum of the diffraction width (FWHM), and θ is the Bragg angle. According to the values calculated from the Scherrer equation, the average crystallite size is found to be ~24 nm. In the XRD patterns of the NMA/GA hybrid cathode, the peak at around 26° is attributed to the (002) of the GA.[51]

The FE-SEM images of NMA cathode active materials at two magnifications (50,000 and 200,000×) are given in Figure 6. The particles are composed of polycrystalline aggregates with very fine morphology. It is seen that the particles calcined at 700 °C have a multisurface morphology, and these particles' diameters are approximately 30−70 nm. With the decreasing calcination temperature of NMA particles, smaller particles are formed. It was observed that NMA nanoparticles formed in a macroporous structure after the calcination process. The uniform distribution of nanoparticles can increase the cathode electrolyte contact surface area and facilitate the transfer of Li$^+$ ions and electrons. The homogeneous distribution of NMA nanoparticles is also confirmed by EDS analysis. As can be seen from the point mapping analysis in Figure 7, a homogeneous distribution of Ni, Al, and Mn is observed. As can be seen from the FESEM image in Figure 8, a 3D graphene aerogel structure with high macro- and mesopores was obtained. A three-dimensional porous structure consisting of micron-sized channels and a cross-linked thin layer of graphene can be observed, and NMA is adhesively dispersed homogeneously on the surface of the graphene.

Because of the low ratio of graphene in the GA/NMA composite structure, the importance of the electrostatic van der Waals forces between NMA particles and graphene
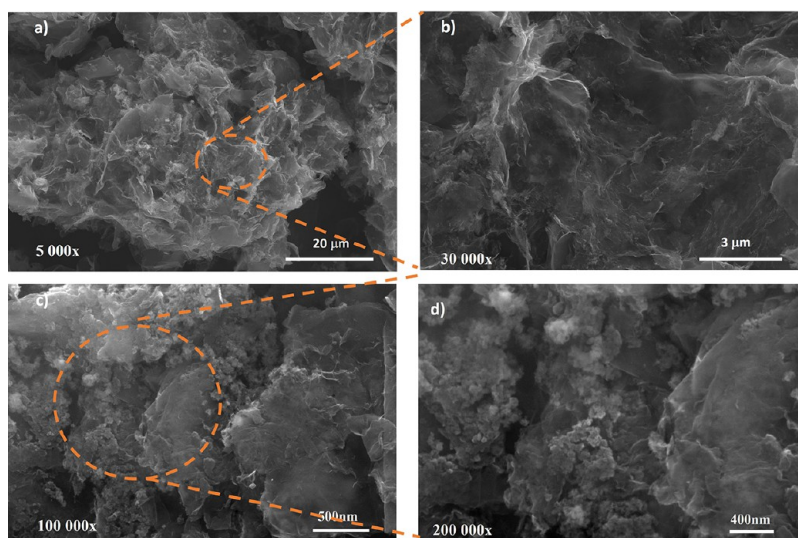

Figure 8. FE-SEM images of the NMA/GA nanocomposite: (a) 5000×, (b) 30,000×, (c) 100,000×, and (d) 200,000×.
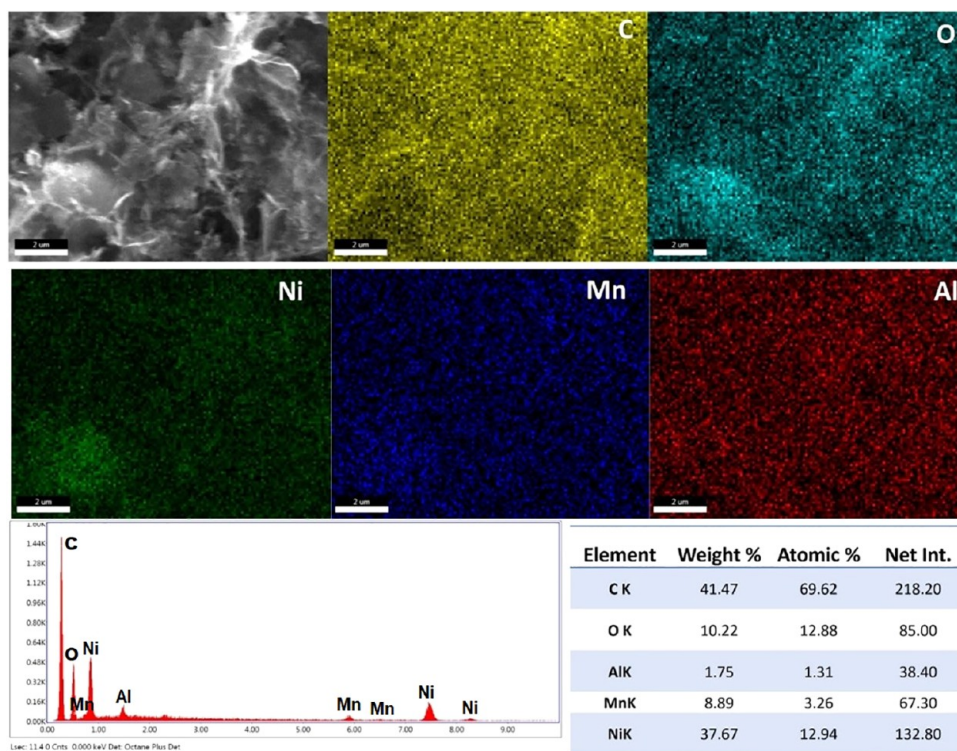
Figure 9. EDS dot-mapping images and EDS analysis of NMA/GA.

becomes important. Porous and interconnected graphene networks expand the cathode/electrolyte interfaces while facilitating lithium ion diffusion during insertion and deinsertion processes.[52] Figure 9 demonstrates the EDS dot-mapping images of the NMA/GA composite electrodes. The particles of NMA are homogeneously distributed between the graphene nanosheets. Ni clusters in Ni-rich layered cathodes are randomly distributed and tend to form more Ni−Ni bonds when interacting with the graphene surface.[53] The three-dimensional structure of the GA area allows more Ni clusters to interact with graphene. The next Ni atom added can bind to the larger cluster, forming more Ni−Ni bonds.[54,55] Thus, clumps only grow on the side of the plate with minor defects. This increase in Ni clusters enables Ni clusters to be seen clearly in the EDS dot-map analysis.

NMA nanoparticles reinforced with transparent graphene are shown in TEM images in Figure 10a,b. NMA is present in the further enlarged interior of the structure. Figure 10c shows the interface of the NMA nanoparticle. The layer thickness of the NMA particle corresponding to the (003) plane was measured as about 0.471 nm. According to the selected field electron diffraction (SAED) model of NMA shown in Figure 10d, the (006) and (003) planes have the same axial direction but different diffraction rings. The simulation of the geometric relationship between the crystal planes ((006), (003), (102), and (104)) of NMA is shown in Figure 10e. Figure 10f,g shows TEM-EDS dot-mapping and TEM-EDS analyses, respectively. According to the analysis, Ni, Mn, Al, O, and C elements in the NMA/GA composite structure were homogeneously distributed, and the composite was successfully synthesized. In addition, the GA layers wrapped tightly the NMA particles.

The FTIR spectra of NMA and NMA/GA shown in Figure 11 were used to define the appearance of the major functional groups in the structure. The band obtained at 540 cm^{-1} expresses the expansion of Li−O in the LiO$_6$ octahedra,[56]

whereas the band around 595 cm^{-1} is attributed to the asymmetric stretching of the M−O bonds in the MO$_6$ octahedra.[57] The peaks at 861 and 1432 cm^{-1} are an indication of the presence of the Ni−O bond.[58] The band 1070 cm^{-1} corresponds to the Li−Mn−O.[59] The peak at 1485 cm^{-1} is attributed to the bond energy of Ni=O, which tends to be close as a result of the homogenization of the valence electrons.[60] All NMA characteristic bands appear weaker in the structure of the NMA/GA composite. In addition, in the FTIR spectra of NMA/GA, none of the oxygen-containing functional groups are visible, indicating that the oxygen-containing functional groups were almost removed in the reduction process and GO is completely converted to graphene. The presence of two peaks at 3010.78 and 2851.64 cm^{-1} indicates the sp3 C−H bond, which proves the presence of hydrocarbons in the structure of the product.[61]

The thermal behavior of the NMA powders and NMA/GA composite was also analyzed by TGA in air atmosphere and is shown in Figure 12a. For pure NMA nanoparticles, the weight remained unchanged even after heating, whereas for the NMA/GA composite, the weight decreased continuously up to 500 °C because of carbon decomposition and CO$_2$ release.[62] The obtained result indicates that the amount of graphene in the composite structure for NMA/GA composite is approximately 30.7%. N$_2$ adsorption/desorption analyses were performed to investigate the porous structural properties of the samples, and its graph is shown in Figure 12b. The pore size distribution calculated by the Barrett−Joyner−Halenda (BJH) desorption cumulative pore size of pure NMA and NMA/GA samples are given as 0.039 and 0.196 cm^3 g^{-1}, respectively. Also, the BET surface areas were measured as 10.1 and 113 m^2 g^{-1} for NMA and NMA/GA, respectively. These results show that the NMA/GA composite significantly increases the surface area thanks to GA. The increased contact area allows these composites to show good electrochemical

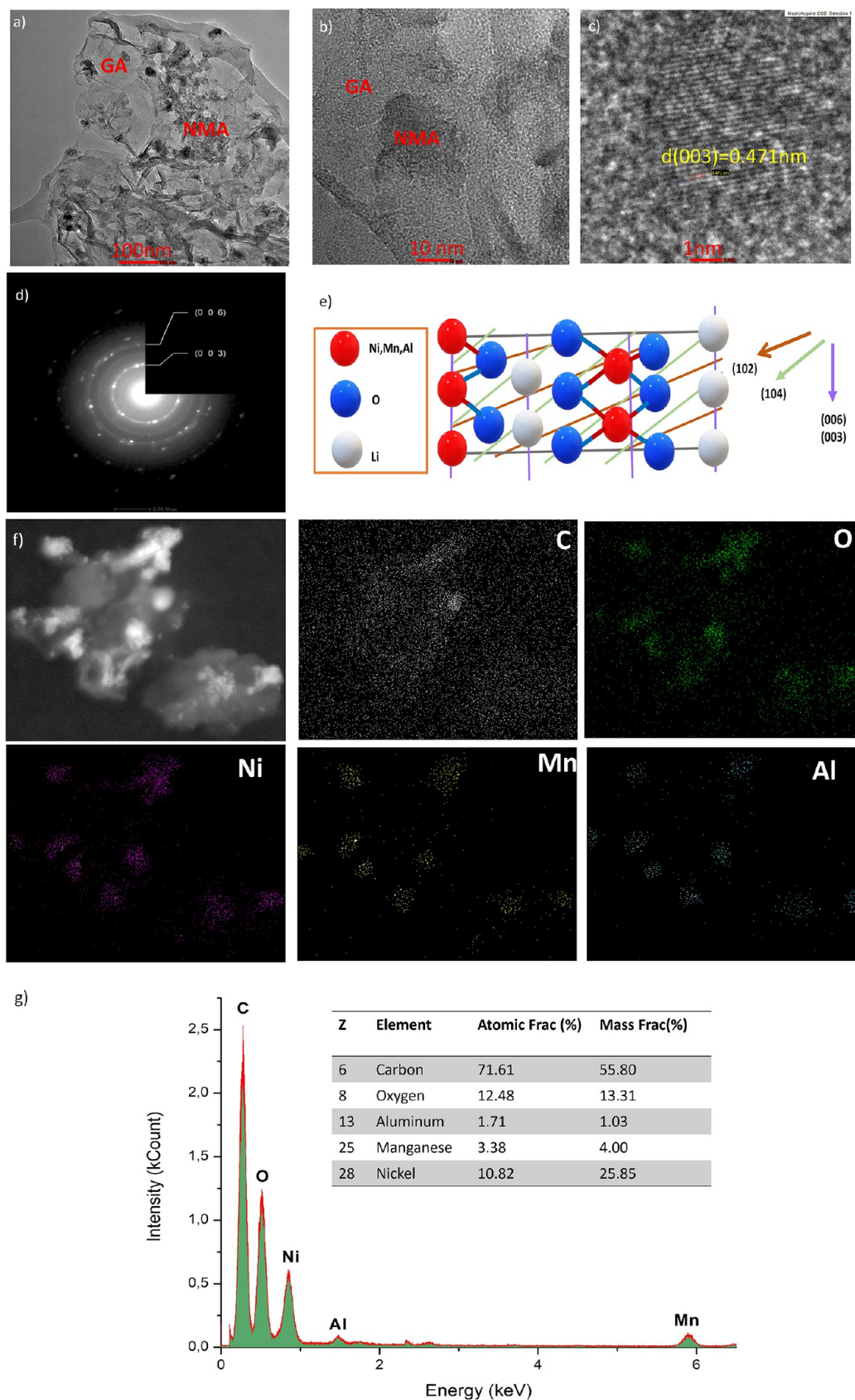**Figure 10.** (a−c) TEM images; (d) SAED pattern of the NMA/GA nanocomposite; (e) atomic structure schematic of the NMA: Li (white), Ni, Mn, Al (red), and O (blue); (f) TEM-EDS dot-mapping images; and (g) TEM-EDS analysis of NMA/GA.

performance even at high current density when used as a cathode in Li-ion batteries.

To investigate the chemical bond and valence value of manganese, aluminum, and nickel, XPS analyses of NMA and
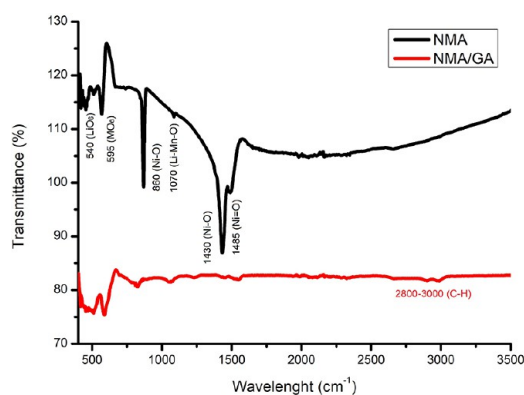
Figure 11. FTIR spectra of the NMA and NMA/GA nanocomposite cathodes.

NMA/GA materials are shown in Figure 13. The energy band values of Li (1s), Al (2p), C (1s), O (1s), Mn (2p), and Ni (2p) for pure NMA are 54.93, 74.03, 285.0, 531.38, 642.24, and 855.51 eV, respectively. For the NMA/GA composite structure, the approximate energy bands corresponding to the elements Li (1s), Al (2p), C (1s), O (1s), Mn (2p), and Ni (2p) are 54, 69.08, 285.10, 532.07, 642.52, and 856.37 eV (Figure 13a). Elemental spectral regions were probed with higher resolution than probes to distinguish specific oxidation states. The Li 1s spectrum at 54.5 eV, the peak corresponding to Li_2CO_3 or LiOH, almost disappears with graphene supplementation (Figure 13b).[63] The amount of Ni in the NMA cathode directly affects the Li ion diffusion coefficient. Li^+/Ni^{2+} exchange usually occurs in this system. During the formation of NMA, unstable Ni^{3+} ions turn into Ni^{2+}, hindering the Li diffusion pathways.[64] Li diffusion decreases because of the Li^+/Ni^{2+} cation mixture formed as a result of the migration of Ni^{2+} ions in the 3b site to the Li^+ in the 3a site.

In addition, Ni^{2+} ions migrate to the surface of the material and destabilize the structure, resulting in reduced rate performance and loss of capacity.[65] Therefore, it is important to understand the relationship between Ni^{2+} concentration and Ni^{3+} concentration to optimize layered NMA materials. Partial oxidation of Ni^{2+} over the surfaces gives lower Ni^{2+}/Ni^{3+} ratios in NMA/GA than in pure NMA due to the slower decomposition reaction of graphene in the structure. In the NMA structure, Ni^{3+} and free Ni^{2+} exist together. Ni^{2+} with a relatively high ion diameter causes cation mixing at the cathode. GA, which is a good absorbent, was used to prevent the free Ni^{3+} from dissolving from the structure. GA

contributes to the improvement of electrochemical performance by relatively preventing the migration of Ni^{2+} from the structure. During graphene production, the hydrophobic structure formed as a result of the oxidation of graphite by OH^- ions and partial functionalization with oxygen (C–OH/C–O/C=O) prevents the contact of Ni-rich oxide structures with hydrophilic lithium hydroxyls/carbonates.[66] In addition, the electrostatic attraction between Ni^{2+} and graphene and the defects in graphene bind with Ni^{2+} to form a strong graphene/NiO composite. Thus, the dissolution and migration of Ni^{2+} are slowed down.[67,68] The Ni $2p_{3/2}$ peak position is recorded at 855.5 eV, whereas the Ni $2p_{1/2}$ peak is at 872.7 eV (Figure 13c). Ni exists as both Ni^{2+} and Ni^{3+}, whereas Al and Mn remain as Al^{3+} and Mn^{4+}, respectively. For the thin spectra of Mn, there are two peaks corresponding to Mn $2p_{1/2}$ and Mn $2p_{3/2}$, respectively (Figure 13d).[69] In the Al 2p spectrum, it can be defined as the AlO_2 bond at 74 eV (Figure 13e),[70] whereas the other peak can be defined as a 72 eV Co 3p element.[71] In O 1s spectra, a single peak is assigned at 531.2 eV of the metal–oxygen bond and Li_2CO_3/LiOH (Figure 13f). As shown in Figure 13g, the C 1s peak at 284.8 eV belongs to hydrocarbon (C–H), and the peak at 288.9 eV corresponds to Li_2CO_3.[72] They represent the three major peaks centered at 284.87, 286.60, and 288.77 eV assigned to the C–H, C–O, and C=O of graphene. After the addition of graphene, the oxygen-containing C–O and C=O peaks were significantly reduced, indicating that the oxygen-based functional groups were greatly reduced.

Cyclic Voltammetry Curves of NMA and NMA/GA Cells. The cyclic voltammogram curves for the pure NMA and NMA/GA cathodes recorded at a scan rate of 0.1 mV s^{-1} from 2.5 to 4.5 V for five cycles are displayed in Figure 14. Ni^{2+}/Ni^{4+} anodic peaks, which occur in NMA and NMA/GA and are formed as a result of the redox reaction, are observed at approximately 4.15 and 4.14 V, respectively. The cathodic peaks are observed at approximately 3.47 and 3.49 V, respectively, formed by the Ni^{4+}/Ni^{2+} redox couples. In addition, the absence of any reduction peak around 3.0 V in the sample indicates that Mn ions remain stable in the +4 oxidation form in the structure.[73,74] Polarization voltages of the NMA and NMA/GA electrodes were calculated according to the CV data. Results calculated from CV analysis are presented in Table 1. According to the data, the NMA electrode has the largest polarization voltage, whereas the NMA/GA hybrid electrode has a lower polarization voltage. This means that the electrode polarization is greatly reduced as a result of the rapid electron transfer property of the conductive GA. High
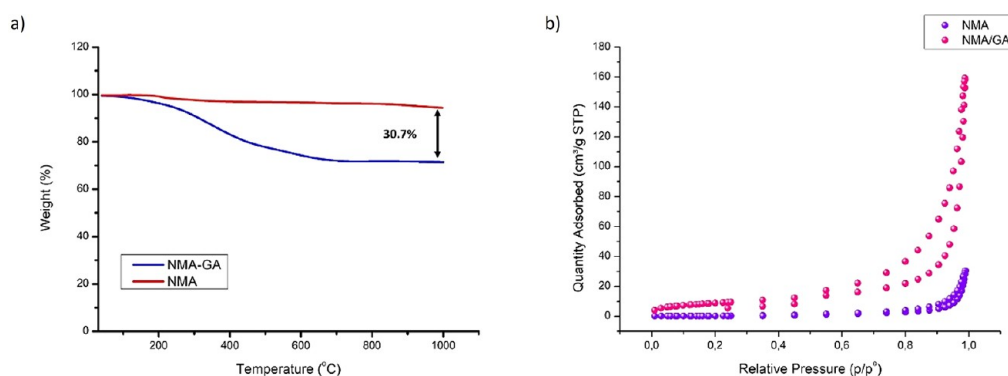

Figure 12. (a) Thermogravimetric curves and (b) nitrogen adsorption/desorption isotherm curves of NMA and NMA/GA.
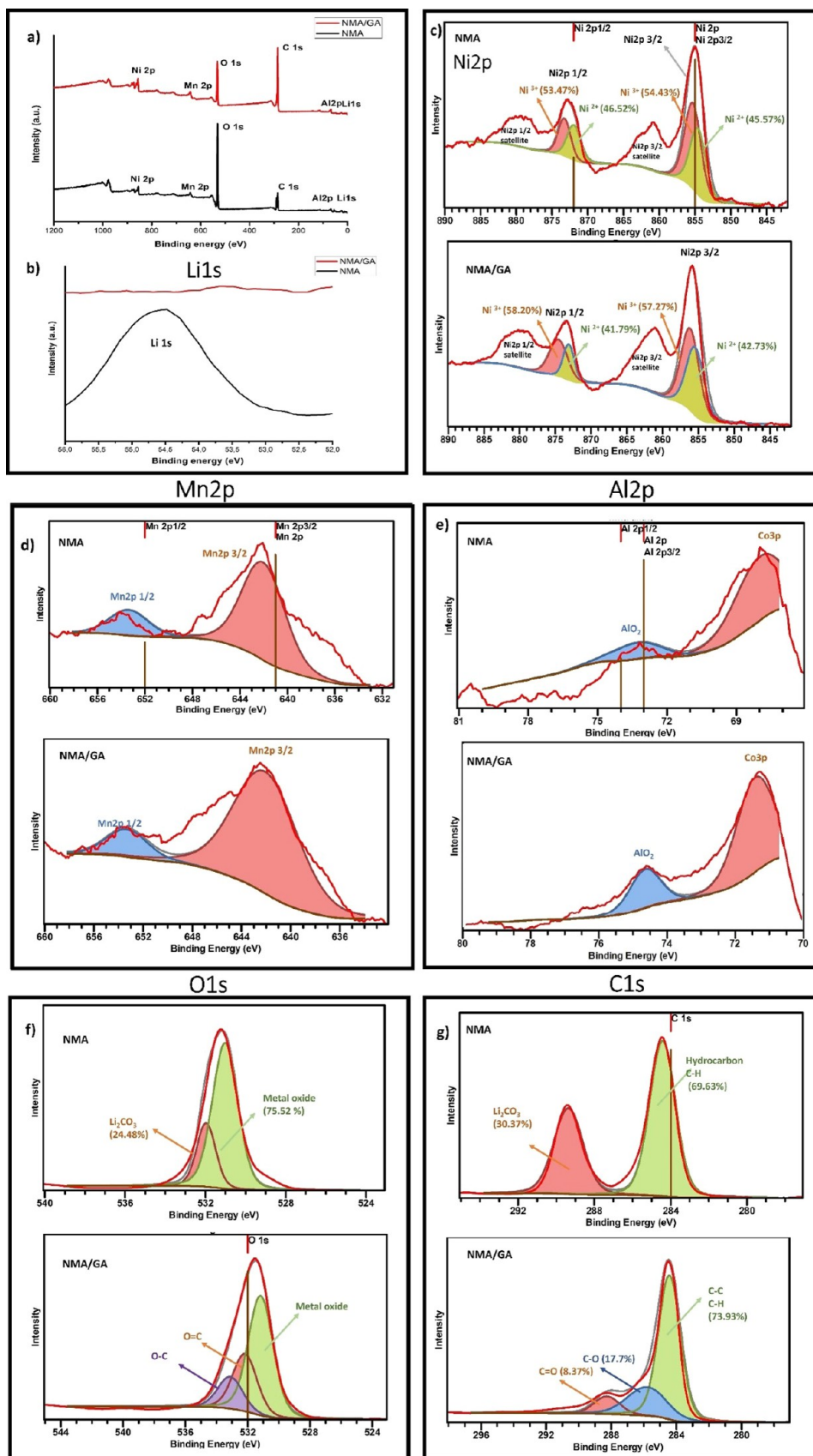
Figure 13. (a) XPS spectra of NMA and NMA/GA. (b−g) High-resolution XPS spectrum of Li 1s, Ni 2p, Mn 2p, O 1s, and C 1s of NMA and NMA/GA.
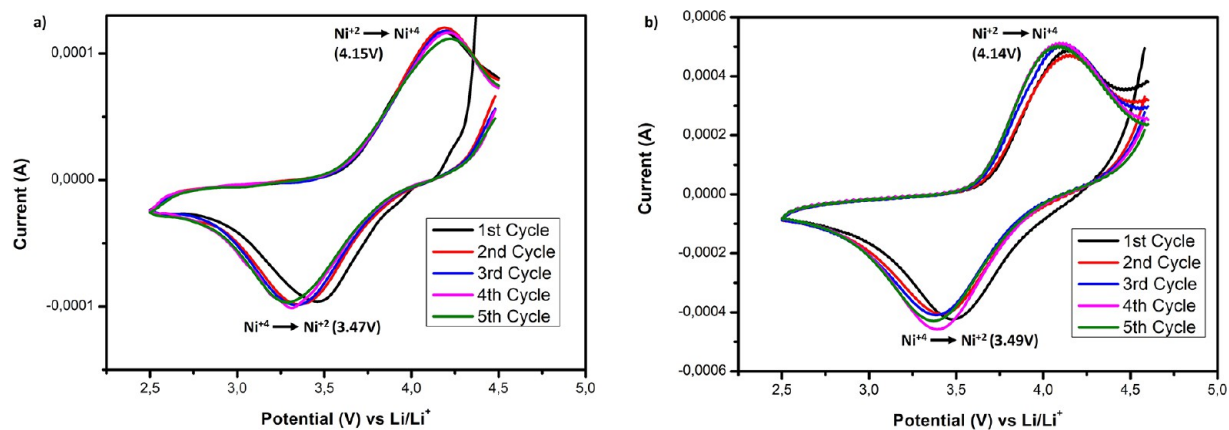
Figure 14. Cyclic voltammetry of (a) NMA and (b) NMA/GA cathodes.

Table 1. Peak Parameters Obtained as a Result of CV Analysis (First Cycle) of NMA and NMA/GA Cathodes

	E_{pa1} (V)	E_{pc1} (V)	ΔE_{p1} (V)
NMA	4.15	3.47	0.68
NMA/GA	4.14	3.49	0.65

polarization voltage is known to have a detrimental effect as it reduces battery performance.

Table 2. R_s, R_{ct}, and Li$^+$ Diffusion Coefficient (DLi$^+$) for the NMA and NMA/GA Half-Cell before the Cycle and after the 50th, 250th, and 500th Cycles

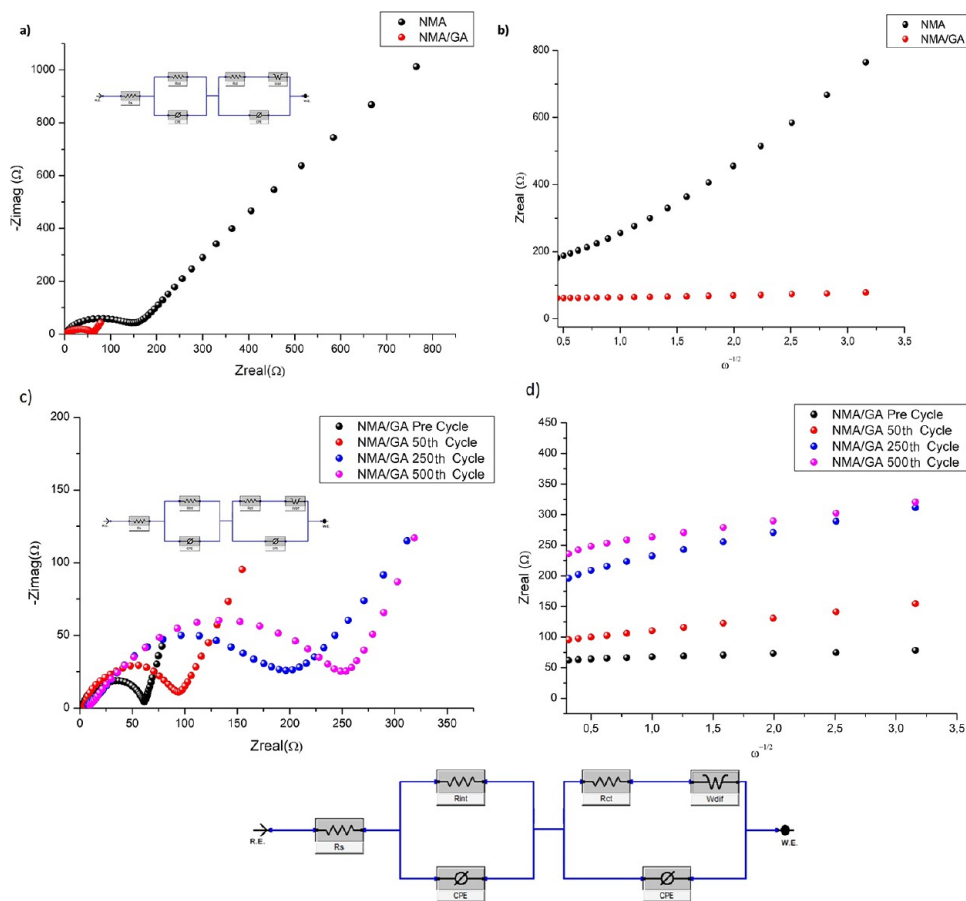| samples	R_S (Ω)	R_{ct} (Ω)	σ	D (cm^2 s^{-1})
NMA	2.816	146.6	71.72	1.71×10^{-9}
NMA/GA precycle	2.717	61.52	17.43	1.27×10^{-8}
NMA/GA 50th cycle	4.31	96.40	20.95	1.19×10^{-8}
NMA/GA 250th cycle	7.904	196.75	31.89	1.13×10^{-8}
NMA/GA 500th cycle	9.36	250.4	41.94	3.39×10^{-9}

Figure 15. (a) Electrochemical impedance spectroscopy curves and (b) diffusion coefficient graphs of pure NMA and NMA/GA. (c) EIS analysis of the NMA/GA half-cell before a cycle and after 50, 250, and 500 cycles. (d) Graph of the relationship between Zreal vs $\omega^{-1/2}$ of the NMA/GA half-cell before a cycle and after 50, 250, and 500 cycles.
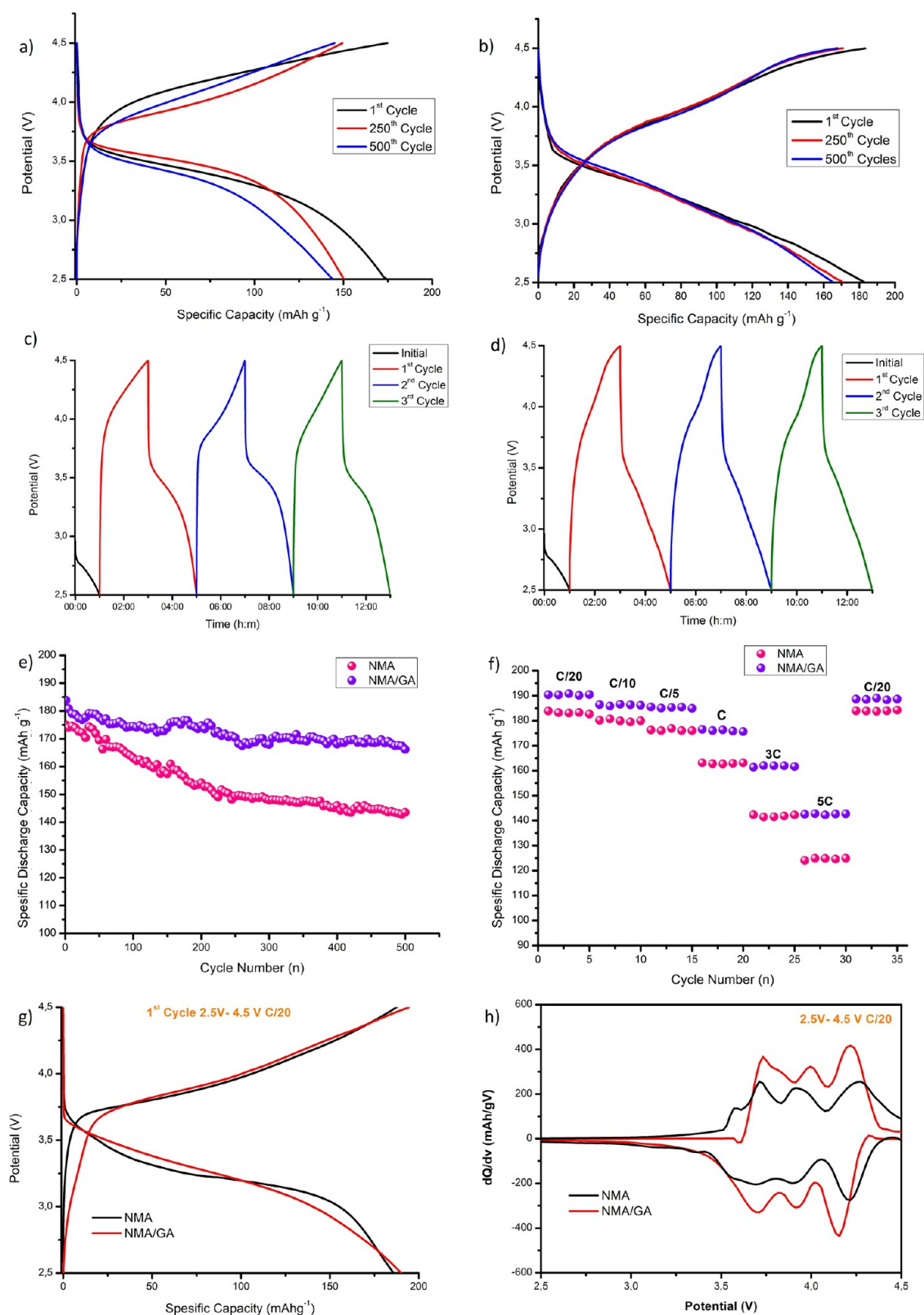
Figure 16. The galvanostatic discharge—charge curves of (a) pure NMA and (b) NMA/GA cathodes, voltage—time curve for the first three cycles of the (c) pure NMA and (d) NMA/GA cathodes, (e) cyclic performance of pure NMA and NMA/GA, (f) specific discharge capacity—cycle number of NMA and NMA/GA cathodes at different charge/discharge rates, (g) electrochemical characterization of NMA and NMA/GA at C/20, and (h) dQ dV^{-1} curves at the first C/20.

Impedance Analysis. To examine in detail the charging/discharging kinetic effects of GA addition to NMA, EIS analysis has also been applied and is shown in Figure 15 with

the frequency range of $10^{-2}-10^{6}$ Hz. The large semicircle indicates the charge transfer resistance of the cell, whereas the lower semicircle represents the diffusion of Li-ions to the active

Table 3. Galvanostatic Discharge−Charge Values of Pure NMA and NMA/GA

samples	1st cycle (mAh g^{-1})	250th cycle (mAh g^{-1})	500th cycle (mAh g^{-1})
NMA	174.8	149.8	143.58
NMA/GA	183.8	170.4	165.08

materials. In addition, the linear line obtained at lower frequencies is attributed to the Warburg impedance, which indicates Li-ion movement between the electrodes.

Nyquist plots were fitted in an equivalent circuit inset in Figure 15a. In the circuit, R_s is related to the ohmic resistance of the electrolyte, R_{int} represents the polarization resistance, and R_{ct} is the charge transfer resistance of the active material interface.[75] The charge transfer resistance of the electrode was obtained as around 145.6 and 61.52 Ω for pure NMA and NMA/GA nanocomposites, respectively. The reduction of the charge transfer resistance could be attributed to GA reinforcements. GA reinforcements significantly improved the electrical conductivity of the NMA cathode.

The Li-ion diffusion coefficient was calculated from the data formed in the impedance spectra.

$$D = \frac{R^2 T^2}{2A^2 n^4 F^4 C^2 \sigma^2}$$

D is the Li-ion diffusion coefficient, T represents the absolute temperature, R indicates the molar gas constant, A depicts the working area of the cathode, n signifies the electron transfer number, F is the Faraday constant, C (1 M LiPF$_6$) denotes the molar density of Li-ion in an electrode, and σ is the slope on the diffusion state of EIS measurement.[76,77] The linear relationship between Z' and $\omega^{-1/2}$ (angular frequency) is displayed in Figure 15b. The Warburg constant σ is obtained from the slope of the simulated curve. The Li-ion diffusion coefficient values calculated for NMA and NMA/GA electrodes according to the aforementioned equation are summarized in Table 2. The results given in Table 2 show that the high conductivity, large specific area, and porosity of the 3D GA structure increased the transfer rate of electrons and accelerated the diffusion of Li$^+$.

The EIS and diffusion coefficient curves of the 50th, 250th, and 500th cycles of the NMA/GA hybrid composite are shown in Figure 15c. Warburg coefficients and Li diffusion coefficient values calculated from the slope of the graph shown in Figure 15d are 1.19×10^{-8}, 1.13×10^{-8}, and 3.39×10^{-9} cm^2 s^{-1} for the 50th, 250th, and 500th cycles, respectively. Although the input and output of Li ions after the cycle decreased the diffusion coefficient values, they did not undergo a significant change thanks to the GA unique structure. It confirms that GAs not only improve the electrical conductivity of the resulting NMA/GA material but also greatly increase the electrochemical activity of NMA nanoparticles.

Charge−Discharge Performance of NMA and NMA/GA Cathodes. In Figure 16, galvanostatic charge/discharge graphs and differential capacity (dQ/dV) of NMA (Figure 16a) and NMA/GA (Figure 16b) positive electrodes are given.

Figure 16c,d shows the voltage−time curve of the first three cycles of the NMA and NMA/GA electrodes. The cells were cycled between 2.5 and 4.5 V at C/2 rate. With an initial capacity of 174.8 mAh g^{-1}, the NMA exhibits a capacity of 143.58 mAh g^{-1} after 500 cycles. Moreover, for the NMA/GA electrode, the initial capacity is 183.8 mAh g^{-1}, which decreases to about 165.08 mAh g^{-1} after 500 cycles (Table 3). Because the high electrical conductivity and 3D porous structure of GA facilitate Li diffusion and relatively prevent the dissolution of Ni^{2+}, a decrease in peak shift and an increase in peak intensities were observed with increasing cycle number. The results show that the pure NMA and NMA/GA samples have shown a stable cycling performance after 500 cycles even though the total capacity losses of NMA and NMA/GA are only 17.86 and 10.18%, respectively (Figure 16e). The obtained data show that the electrochemical cycling performance of NMA/GA has been significantly improved. Thanks to the nanosize of NMA and 3D conductive structure and larger surface of the GA, it provides more paths for Li$^+$ ion movement in the electrode/electrolyte interface and reduces polarization. Figure 16f compares the capacitances for NMA and NMA/GA cathodes in the 2.5−4.5 V range at different C rates of C/20, C/10, C/5.1C, 3C, and 5C, respectively. The NMA/GA positive electrode exhibits a capacity value of 188.5 mAh g^{-1} when the current ratio is reduced to C/20 after 30 cycles. This can be attributed to their porous nanostructures, which provide a larger surface area to store more Li ions, buffer the large volume change to some extent, and simultaneously reduce the diffusion length of Li$^+$. The NMA/GA composite with a 3D porous conductive architecture provides outstanding advantages such as better rate capability over pure NMA at different ratios. Especially at 3C and 5C, the differences between the two cathodes are more pronounced. This is due to decreased polarization and increased Li$^+$ diffusion by GA. The NMA/GA cathode showed average capacities of 190.2, 186.3, 185.2, 176.2, 161.2, and 142.6 mAh g^{-1} at current densities of C/20, C/10, 0.2C, 1C, 3C, and 5C, respectively (Table 4). To better understand the electrochemical behavior, galvanostatic charge/discharge analysis results at C/20 rate of NMA and NMA/GA electrodes are presented in Figure 16g. NMA and NMA/GA electrodes showed a discharge capacity value of 187.9 and 194.4 mAh g^{-1}, respectively, at the end of the first cycle. The differential capacity curves dQ/dV obtained from these curves are shown in Figure 16h. As can be seen from the figure, because of the high electrical and ionic conductivity of graphene, the NMA/GA composite showed less polarization difference and higher electrode reaction reversibility than the NMA electrode.

Structural Characterization of Postcycle Electrodes. Aging leads to capacitance and power reduction and electrode degradation in LIBs. The main cause of degradation is related to material loss during the insertion/deinsertion of the active material. Such losses may occur over time or cyclically. A potential cause of loss of capacity during the electrochemical cycle is irreversible mechanical failures. Figure 17 shows XRD patterns of the NMA/GA electrode charged at the 50th, 250th,

Table 4. Specific Discharge Capacity-Cycle Numbers of NMA and NMA/GA Electrodes at Different Charge/Discharge Rates

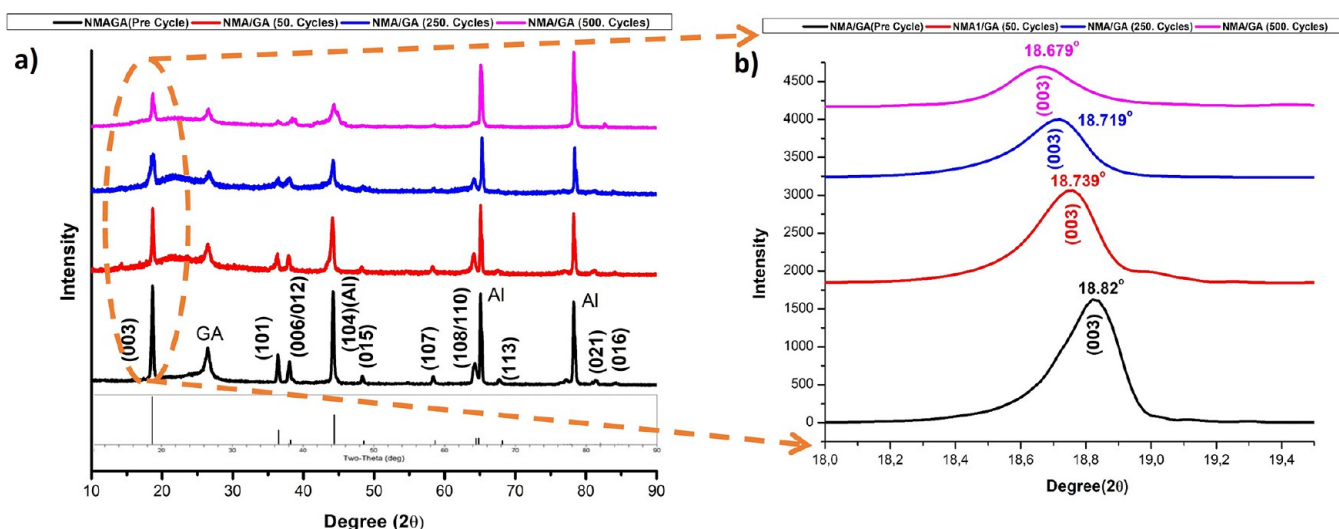| samples	C/20 (mAh g^{-1})	C/10 (mAh g^{-1})	C/5 (mAh g^{-1})	C (mAh g^{-1})	3C (mAh g^{-1})	5C (mAh g^{-1})	C/20 (mAh g^{-1})
NMA	185.8	179.9	176.8	160.8	142.2	124.2	184.2
NMA/GA	190.2	186.3	185.2	176.2	161.2	142.6	188.5

Figure 17. (a) XRD analysis of NMA/GA cathodes precycle and at the 50th, 250th, and 500th cycles. (b) Extended views of X-ray diffraction data [003] of the NMA/GA precycle and NMA/GA at the 50th, 250th, and 500th cycles.

Table 5. The Lattice Parameters of NMA/GA Electrodes Precycle and at the 50th, 250th, and 500th Cycles

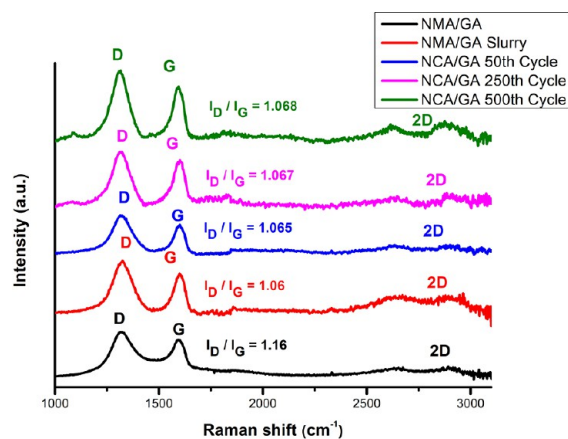|	2θ	$d_{(003)}$	$d_{(110)}$	a	c	c/a	degree of crystallinity
NMA/GA precycle	18.82	4.7114	1.4321	2.8642	14.1342	4.9347	380.2281369
NMA/GA 50th cycle	18.739	4.7316	1.4320	2.864	14.1948	4.9546	362.318840
NMA/GA 250th cycle	18.719	4.7365	1.4280	2.856	14.2095	4.9753	218.4713376
NMA/GA 500th cycle	18.679	4.7464	1.4260	2.852	14.2392	4.989	199.8601399

Figure 18. Raman spectra of the NMA/GA and NMA/GA slurry after the 50th, 250th, and 500th cycles of NMA/GA cathodes.

and 500th cycles from 2.5 to 4.5 V against Li/Li$^+$. All samples are indexed to a hexagonal structure of type α-NaFeO$_2$ with lattice parameters. In the figure, the peaks (006/012) and (108/110) at 2θ = 38 and 65°, respectively, are clearly defined, indicating that the NMA particles in all samples have a layered structure. Also, a relatively broad peak observed in the range of 2θ = 25 to 28° is the characteristic peak of GA. Because the obtained electrodes were plastered on an aluminum foil, the 44, 65, and 78° peaks seen in all XRD analyses belong to the aluminum peaks.[78] During the charge−discharge process, an amorphous structure between 20 and 25° emerged in the structure. XRD measurements show the difference in the lattice parameters a and c due to the volume change in the unit cell as the cycle continues. The lattice parameters initially decrease slightly compared to the precycled cathodes. A

shrinkage in the "a" lattice parameter is also obtained as a result of the decrease in the bond distances and oxidation nature of TMs.[79]

The unit cell expands in the c-direction for the lattice parameter representing the distance between transition metal layers when lithium is removed as a result of increased electrostatic repulsion between oxygen atoms. This clearly indicates that lattice expansion has occurred in the lattice. The decrease in peak intensity is associated with lower crystallinity in the structure. The degree of crystallization was calculated using Imax and β data (Table 5). Here, Imax represents the maximum intensity of the peak, and β represents the FWHM value. Figure 17b shows that as the cell ages (003), the oxide peak moves to a smaller 2θ; this behavior is consistent with the broadening of the c-axis parameter resulting from the removal of Li-ions from the oxide.

To examine the structural behavior during the cycling, the Raman analysis of the NMA/GA electrode at the precycle and at the 50th, 250th, and 500th cycles is shown in Figure 18. The G band at ∼1350 cm^{-1} and plane of all sp2 carbon atom pairs are attributed to intracranial stress.[80] D bands appearing at approximately 1620 cm^{-1} are associated with defect-induced Raman features. The degree of deformation in the GA is determined using the band density ratio of I_D and I_G (I_D/I_G). The I_D/I_G ratio was calculated as 1.16 for the NMA/GA composite sample, and this calculated value shows that most of the oxygen-containing functional groups in the graphene oxide structure were removed from the structure. The I_D/I_G ratio for the precycle slurry for the NMA/GA sample was calculated as 1.06. Because the positive electrode contains super P carbons, this value is lower than expected for the GA-assisted composite. Then, after the 50th, 250th, and 500th cycles, the I_D/I_G ratios were calculated, and these values were given as 1.065, 1.067, and 1.068, respectively. As the number of cycles
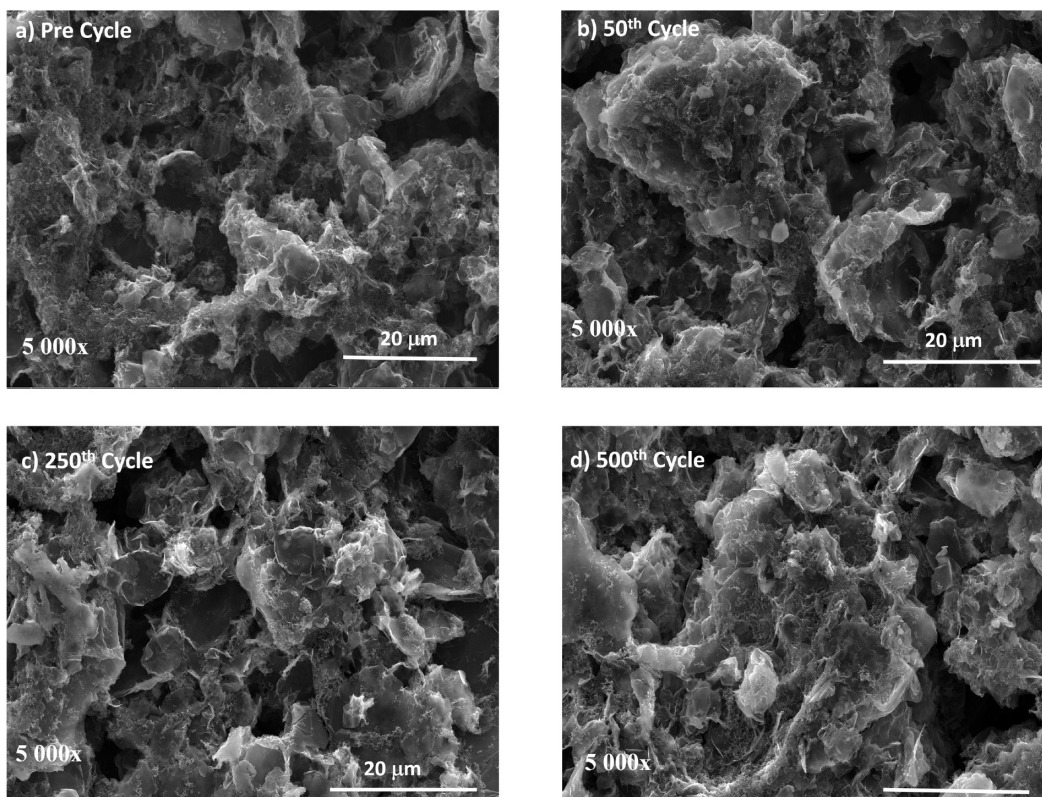
Figure 19. FE-SEM images of the NMA/GA nanocomposite cathodes (a) at precycle and after the (b) 50th, (c) 250th, and (d) 500th cycles at 5000× magnification.

Figure 20. FE-SEM images of the NMA/GA nanocomposite cathodes (a) at precycle and after the (b) 50th, (c) 250th, and (d) 500th cycles at 100,000× magnifications.

continues, the I_D/I_G ratio increases as the positive electrode undergoes structural irregularities.

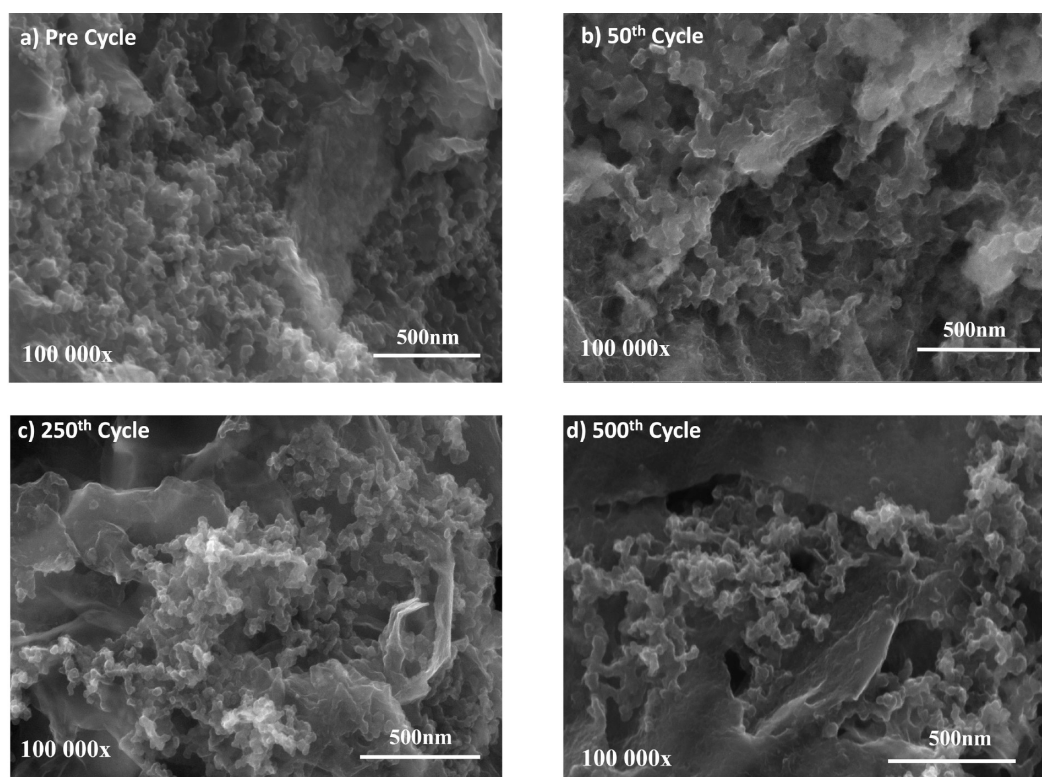FE-SEM images of the NMA/GA electrode after the 50th, 250th, and 500th cycles of charge/discharge are given in
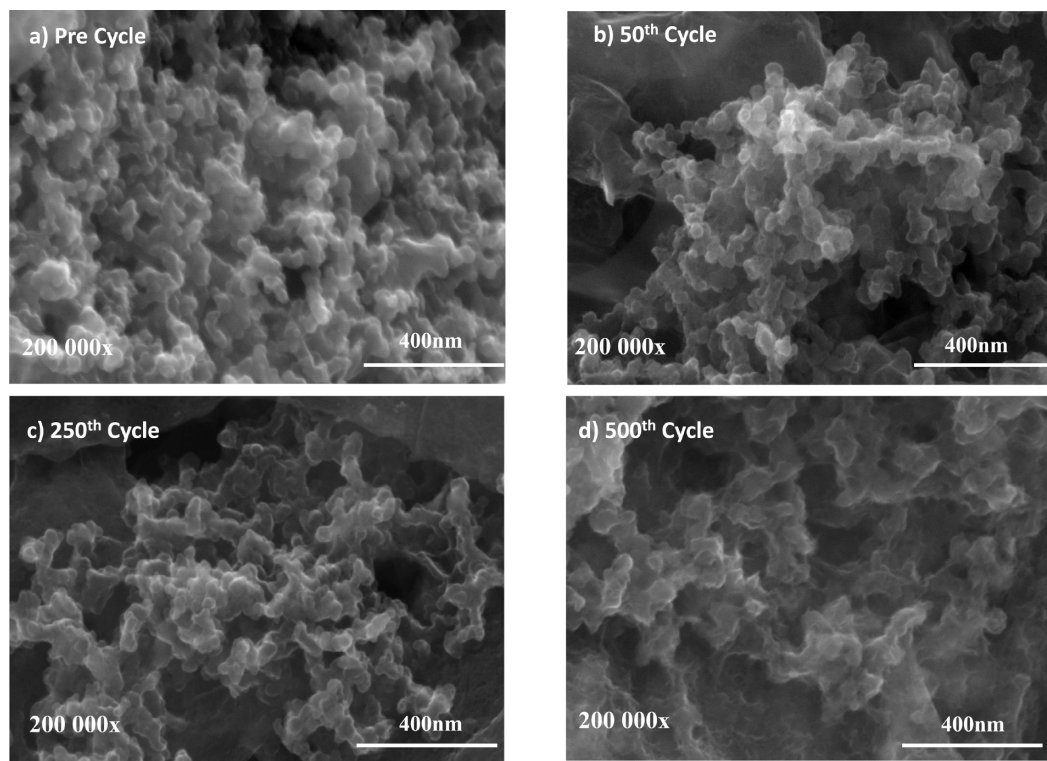
Figure 21. FE-SEM images of the NMA/GA nanocomposite cathodes (a) at precycle and after the (b) 50th, (c) 250th, and (d) 500th cycles at 200,000× magnifications.
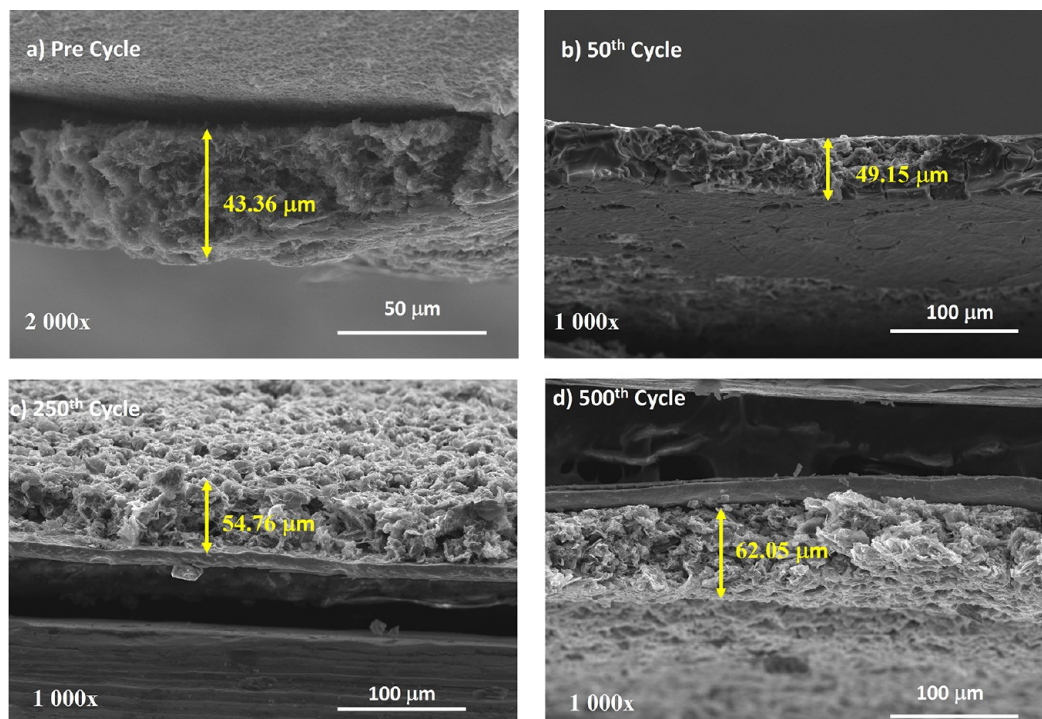

Figure 22. FE-SEM images of the section thickness measurements of the electrodes of the NMA/GA sample (a) before the cycle and after the (b) 50th, (c) 250th, and (d) 500th cycles.

Figures 19−21. After the 50th cycle, it was observed that there was no crack on the electrode surface and the electrode preserved its structural integrity. After the 250th cycle, there was no morphology change in the electrode structure, and no crack formation was observed. At the end of the 500th cycle, the morphology differences in the electrode structure are not different, so the structural integrity of the electrode is not impaired. Moreover, there was no deterioration in the structure of NMA/GA cathodes, and agglomeration occurred in NMA particles as the number of cycles increased. In addition, it is

thought that salt residue is formed in the structure as a result of the electrolyte remaining on the electrodes.

In Figure 22, FE-SEM images of the section thickness measurements of the NMA/GA sample at precycle and at the 50th, 250th, and 500th cycles are given, and their thicknesses were measured as 43.36, 49.15, 54.76, and 62.05 μm, respectively. The reasons for the increase in thickness can be considered as the c/a change, the fact that all lithium ions do not return to the main structure during the charge–discharge process, and the increase in the distance between the graphene layers.

CONCLUSIONS

In this study, $LiNi_{0.8}Mn_{0.15}Al_{0.05}$, which does not contain cobalt and has a cheap high Ni ratio, was produced. NMA nanoparticles were synthesized via the sol–gel method as a cathode active material. GA was prepared using ascorbic acid as the reducing agent. Then, synthesized NMA powders were dispersed with ultrasonication in the GA solution. The successfully prepared $LiNi_{0.8}Mn_{0.15}Al_{0.05}$ nanoparticles were supported by a 3D porous and conductive GA skeletal network. Thanks to the new composite created, the contact area between the cathode and the electrolyte has increased and the conductivity of the material has been improved. According to XPS analysis, it was observed that the valences of Al^{3+} and Mn^{4+} used did not change and Ni was found as Ni^{2+} and Ni^{3+}. As can be concluded from the data, the residual lithium compound was removed by rinsing the particles after the sol–gel process. The superior cycle stability of the NMA/GA cathode remained up to 165.08 mAh g^{-1} after 500 cycles. Impedance tests have also proven that GA reinforcement has a positive effect on the electrochemical properties. The a and c lattice parameters were calculated after the 50th, 250th, and 500th cycles based on the XRD results, and it was observed that the c lattice parameter increased during cycling. The decrease in the a parameter is related to the oxidation of the transition metals. In general, the structure of the cathode material with high Ni content did not deteriorate. It was observed that as the number of cycles applied to the electrodes increased, the I_D/I_G ratio of the electrodes increased, and so the structural defects in the electrode increased.

AUTHOR INFORMATION

Corresponding Author

Deniz Kuruahmet − *Engineering Faculty, Department of Metallurgical & Materials Engineering, Sakarya University, 54187 Adapazari, Sakarya, Turkey;* ⊙ orcid.org/0000-0002-4749-682X; Email: deniz.nalci2@ogr.sakarya.edu.tr

Authors

Aslihan Guler − *Engineering Faculty, Department of Metallurgical & Materials Engineering, Sakarya University, 54187 Adapazari, Sakarya, Turkey;* ⊙ orcid.org/0000-0002-5155-2214

Sidika Yildirim − *Engineering Faculty, Department of Metallurgical & Materials Engineering, Sakarya University, 54187 Adapazari, Sakarya, Turkey; Dr. Engin Pak Cumayeri Vacational School, Duzce University, 81700 Cumayeri, Duzce, Turkey*

Mustafa Mahmut Singil − *Engineering Faculty, Department of Metallurgical & Materials Engineering, Sakarya University, 54187 Adapazari, Sakarya, Turkey*

Hatice Güngör − *Engineering Faculty, Department of Metallurgical & Materials Engineering, Sakarya University, 54187 Adapazari, Sakarya, Turkey*

Esma Uzun − *Engineering Faculty, Department of Metallurgical & Materials Engineering, Sakarya University, 54187 Adapazari, Sakarya, Turkey*

Engin Alkan − *Engineering Faculty, Department of Metallurgical & Materials Engineering, Sakarya University, 54187 Adapazari, Sakarya, Turkey*

Mehmet Oguz Guler − *Engineering Faculty, Department of Metallurgical & Materials Engineering, Sakarya University, 54187 Adapazari, Sakarya, Turkey*

Hatem Akbulut − *Engineering Faculty, Department of Metallurgical & Materials Engineering, Sakarya University, 54187 Adapazari, Sakarya, Turkey*

Complete contact information is available at:
https://pubs.acs.org/10.1021/acsomega.2c08281

Author Contributions

All authors contributed equally.

Notes

The authors declare no competing financial interest.

ACKNOWLEDGMENTS

REFERENCES

(1) Xie, Z.; Zhang, Y.; Yuan, A.; Xu, J. Effects of lithium excess and SnO_2 surface coating on the electrochemical performance of $LiNi_{0.8}Co_{0.15}Al_{0.05}O_2$ cathode material for Li-ion batteries. *J. Alloys Compd.* **2019**, *787*, 429−439.

(2) Goodenough, J. B.; Park, K. S. The Li-ion rechargeable battery: a perspective. *J. Am. Chem. Soc.* **2013**, *135*, 1167−1176.

(3) Tang, F.; Jiang, T.; Tan, Y.; Xu, X.; Zhou, Y. Preparation and electrochemical performance of Silicon@Graphene aerogel composites for lithium-ion batteries. *J. Alloys Compd.* **2021**, *854*, No. 157135.

(4) Xu, C.; Reeves, P. J.; Jacquet, Q.; Grey, C. P. Phase behavior during electrochemical cycling of Ni-rich cathode materials for Li-ion batteries. *Adv. Energy Mater.* **2021**, *11*, 7.

(5) Çetin, B.; Camtakan, Z.; Yuca, N. Synthesis and characterization of Li-rich cathode material for lithium ion batteries. *Mater. Lett.* **2020**, 273.

(6) Liu, W.; Li, J.; Li, W.; Xu, H.; Zhang, C.; Qiu, X. Inhibition of transition metals dissolution in cobalt-free cathode with ultrathin robust interphase in concentrated electrolyte. *Nat. Commun.* **2020**, *11*, 1.

(7) Muralidharan, N.; Essehli, R.; Hermann, R. P.; Amin, R.; Jafta, C.; Zhang, J.; Liu, J.; Du, Z.; Meyer, H. M.; Self, E.; Nanda, J.; Belharouak, I. Lithium iron aluminum nickelate, $LiNi_xFe_yAl_zO_2$—new sustainable cathodes for next-generation cobalt-free Li-ion batteries. *Adv. Mater.* **2020**, *32*, 34.

(8) Chikkannanavar, S. B.; Bernardi, D. M.; Liu, L. A Review of blended cathode materials for use in Li-ion batteries. *J. Power Sources* **2014**, *248*, 91−100.

(9) Tsai, P. C.; Wen, B.; Wolfman, M.; Choe, M. J.; Pan, M. S.; Su, L.; Thornton, K.; Cabana, J.; Chiang, Y. M. Single-particle measurements of electrochemical kinetics in NMC and NCA cathodes for Li-ion batteries. *Energy Environ. Sci.* **2018**, *11*, 860−871.

(10) Xia, Y.; Zheng, J.; Wang, C.; Gu, M. Designing principle for Ni-rich cathode materials with high energy density for practical applications. *Nano Energy* **2018**, *49*, 434−452.

(11) Zhang, M.; Dong, L.; Zhang, C.; Yin, F.; Peng, H.; Wang, G. Heterogeneous nucleation of Li_3VO_4 regulated in dense graphene

aerogel for lithium ion capacitors. *J. Power Sources* **2020**, *468*, No. 228364.

(12) Karthikeyan, K.; Amaresh, S.; Lee, G. W.; Aravindan, V.; Kim, H.; Kang, K. S.; Kim, W. S.; Lee, Y. S. Electrochemical performance of cobalt free, $Li_{1.2}(Mn_{0.32}Ni_{0.32}Fe_{0.16})O_2$ cathodes for lithium batteries. *Electrochim. Acta* **2012**, *68*, 246−253.

(13) Zhou, Y.; Liu, Q.; Liu, D.; Xie, H.; Wu, G.; Huang, W.; Tian, Y.; He, Q.; Khalil, A.; Haleem, Y. A.; Xiang, T.; Chu, W.; Zou, C.; Song, L. Carbon-coated MoO_2 dispersed in three-dimensional graphene aerogel for lithium-ion battery. *Electrochim. Acta* **2015**, *174*, 8−14.

(14) Takanashi, S.; Abe, Y. Improvement of the electrochemical performance of an NCA positive-electrode material of lithium ion battery by forming an Al-rich surface layer. *Ceram. Int.* **2017**, *43*, 9246−9252.

(15) Li, W.; Lee, S.; Manthiram, A. high-nickel NMA: a cobalt-free alternative to NMC and NCA cathodes for lithium-ion batteries. *Adv. Mater.* **2020**, *32*.

(16) Tsutomo, O.; Yoshinari, M. Layered lithium insertion material of $LiNi_{1/2}Mn_{1/2}O_2$: A possible alternative to $LiCoO_2$ for advanced lithium-ion batteries. *Chem. Lett.* **2001**, *30*, 744−745.

(17) Croy, J. R.; Long, B. R.; Balasubramanian, M. A path toward cobalt-free lithium-ion cathodes. *J. Power Sources* **2019**, *440*, No. 227113.

(18) Li, Z.; Wang, C.; Ma, X.; Yuan, L.; Sun, J. Synthesis, structures and electrochemical properties of $Li_XNi_{1-X}O$. *Mater. Chem. Phys.* **2005**, *91*, 36−39.

(19) Yan, P.; Zheng, J.; Lv, D.; Wei, Y.; Zheng, J.; Wang, Z.; Kuppan, S.; Yu, J.; Luo, L.; Edwards, D.; Olszta, M.; Amine, K.; Liu, J.; Xiao, J.; Pan, F.; Chen, G.; Zhang, J. G.; Wang, C. M. Atomic-resolution visualization of distinctive chemical mixing behavior of Ni, Co, and Mn with Li in layered lithium transition-metal oxide cathode materials. *Chem. Mater.* **2015**, *27*, 5393−5401.

(20) Xu, J.; Hu, E.; Nordlund, D.; Mehta, A.; Ehrlich, S. N.; Yang, X. Q.; Tong, W. Understanding the degradation mechanism of lithium nickel oxide cathodes for Li-ion batteries. *ACS Appl. Mater. Interfaces* **2016**, *8*, 31677−31683.

(21) Torchio, R.; Marini, C.; Kvashnin, Y. O.; Kantor, I.; Mathon, O.; Garbarino, G.; Meneghini, C.; Anzellini, S.; Occelli, F.; Bruno, P.; Dewaele, A.; Pascarelli, S. Structure and magnetism of cobalt at high pressure and low temperature. *Phys. Rev. B* **2016**, *94*, No. 024429.

(22) https://tr.investing.com/commodities/cobalt

(23) https://tradingeconomics.com/commodity/cobalt

(24) https://tr.investing.com/commodities/nickel

(25) https://tr.investing.com/commodities/aluminum

(26) Zheng, J.; Teng, G.; Xin, C.; Zhuo, Z.; Liu, J.; Li, Q.; Hu, Z.; Xu, M.; Yan, S.; Yang, W.; Pan, F. Role of superexchange interaction on tuning of Ni/Li disordering in layered $Li(Ni_xMn_yCo_z)O_2$. *J. Phys. Chem. Lett.* **2017**, *8*, 5537−5542.

(27) Wang, Y.; Ma, L.; Xi, X.; Nie, Z.; Zhang, Y.; Wen, X.; Lyu, Z. Regeneration and characterization of $LiNi_{0.8}Co_{0.15}Al_{0.05}O_2$ cathode material from spent power lithium-ion batteries. *Waste Manage.* **2019**, *95*, 192−200.

(28) Bianchini, M.; Roca-Ayats, M.; Hartmann, P.; Brezesinski, T.; Janek, J. There and Back Again—The journey of $LiNiO_2$ as a cathode active material. *Am. Ethnol.* **2019**, *58*, 10434−10458.

(29) Hong, C.; Leng, Q.; Zhu, J.; Zheng, S.; He, H.; Li, Y.; Liu, R.; Wan, J.; Yang, Y. Revealing the Correlation between Structural Evolution and Li+diffusion Kinetics of nickel-rich cathode materials in Li-ion batteries. *J. Mater. Chem. A* **2020**, *8*, 8540−8547.

(30) Rougier, A.; Gravereau, P.; Delmas, C. Optimization of the composition of the $Li_{1-z}Ni_{1+z}O_2$ electrode materials: structural, magnetic, and electrochemical studies. *J. Electrochem. Soc.* **1996**, *143*, 1168−1175.

(31) Li, H.; Cormier, M.; Zhang, N.; Inglis, J.; Li, J.; Dahn, J. R. Is cobalt needed in Ni-rich positive electrode materials for lithium ion batteries? *J. Electrochem. Soc.* **2019**, *166*, 429−439.

(32) Bak, S. M.; Hu, E.; Zhou, Y.; Yu, X.; Senanayake, S. D.; Cho, S. J.; Kim, K. B.; Chung, K. Y.; Yang, X. Q.; Nam, K. W. Structural

changes and thermal stability of charged $LiNi_xMn_yCo_zO_2$ cathode materials studied by combined in situ time-resolved XRD and mass spectroscopy. *ACS Appl. Mater. Interfaces* **2014**, *6*, 22594−22601.

(33) Kim, Y.; Seong, W. M.; Manthiram, A. Cobalt-free, high-nickel layered oxide cathodes for lithium-ion batteries: progress, challenges, and perspectives. *Energy Storage Mater.* **2021**, *34*, 250−259.

(34) Shaju, K. M.; Rao, G. V. S.; Chowdari, B. V. R. Performance of layered $Li(Ni_{1/3}Co_{1/3}Mn_{1/3})O_2$ as cathode for li-ion batteries. *Electrochim. Acta* **2002**, *48*, 145−151.

(35) Zheng, J.; Liu, T.; Hu, Z.; Wei, Y.; Song, X.; Ren, Y.; Wang, W.; Rao, M.; Lin, Y.; Chen, Z.; Lu, J.; Wang, C.; Amine, K.; Pan, F. Tuning of thermal stability in layered $Li(Ni_xMn_yCo_z)O_2$. *J. Am. Chem. Soc.* **2016**, *138*, 13326−13334.

(36) Yoshitake, M.; Yagyu, S.; Chikyow, T. A Numerical formula for general prediction of interface bonding between alumina and aluminum-containing alloys. *Int. J. Met.* **2014**, *2014*, 1−11.

(37) Tsutomo, O.; Yoshinari, M. Layered Lithium insertion material of $LiCo_{1/3}Ni_{1/3}Mn_{1/3}O_2$ for lithium *batteries*. *Chem. Lett.* **2001**, *30*, 642.

(38) Chen, C. H.; Liu, J.; Stoll, M. E.; Henriksen, G.; Vissers, D. R.; Amine, K. Aluminum-doped lithium nickel cobalt oxide electrodes for high-power lithium-ion batteries. *J. Power Sources* **2004**, *128*, 278−285.

(39) Ali, A.; Liang, F.; Zhu, J.; Shen, P. K. The role of graphene in rechargeable lithium batteries: Synthesis, functionalization, and perspectives. *Nano Mater. Sci.* **2022**, DOI: 10.1016/j.nanoms.2022.07.004.

(40) Kim, H.; Park, K. Y.; Hong, J.; Kang, K. All-graphene-battery: bridging the gap between supercapacitors and lithium ion batteries. *Sci. Rep.* **2014**, *4*, 5278.

(41) Yang, H.; Zhang, C.; Meng, Q.; Cao, B.; Tian, G. Pre-lithiated manganous oxide/graphene aerogel composites as anode materials for high energy density lithium ion capacitors. *J. Power Sources* **2019**, *431*, 114−124.

(42) Ren, H.; Shi, X.; Zhu, J.; Zhang, Y.; Bi, Y.; Zhang, L. Facile synthesis of N-doped graphene aerogel and its application for organic solvent adsorption. *J. Mater. Sci.* **2016**, *51*, 6419−6427.

(43) Xie, X.; Chen, S.; Sun, B.; Wang, C.; Wang, G. 3D networked tin oxide/graphene aerogel with a hierarchically porous architecture for high-rate performance sodium-ion batteries. *ChemSusChem* **2015**, *8*, 2948−2955.

(44) Zeng, M.; Wang, W. L.; Bai, X. D. Preparing three-dimensional graphene architectures: review of recent developments. *Chin. Phys. B* **2013**, *22*, No. 098105.

(45) Zhu, C.; Han, T. Y. J.; Duoss, E. B.; Golobic, A. M.; Kuntz, J. D.; Spadaccini, C. M.; Worsley, M. A. Highly compressible 3D periodic graphene aerogel microlattices. *Nat. Commun.* **2015**, *6*, 6962.

(46) Du, G.; Xi, Y.; Tian, X.; Zhu, Y.; Zhou, Y.; Deng, C.; Zhu, H.; Natarajan, A. One-step hydrothermal synthesis of 3D porous microspherical $LiFePO_4$/Graphene Aerogel composite for lithium-ion batteries. *Ceram. Int.* **2019**, *45*, 18247−18254.

(47) Tian, X.; Zhu, Y.; Tang, Z.; Xie, P.; Natarajan, A.; Zhou, Y. Ni-rich $LiNi_{0.6}Co_{0.2}Mn_{0.2}O_2$ nanoparticles enwrapped by a 3D graphene aerogel network as a high-performance cathode material for Li-ion batteries. *Ceram. Int.* **2019**, *45*, 22233−22240.

(48) Ohzuku, T.; Ueda, A.; Nagayama, M. Electrochemistry and structural chemistry of $LiNiO_2$ (R3m) for 4 volt secondary lithium cells. *J. Electrochem. Soc.* **1993**, *140*, 1862.

(49) Li, J.; Liang, G.; Zheng, W.; Zhang, S.; Davey, K.; Pang, W. K.; Guo, Z. Addressing cation mixing in layered structured cathodes for lithium-ion batteries: A critical review. *Nano Mater. Sci.* **2022**, DOI: 10.1016/j.nanoms.2022.09.001.

(50) Bishnoi, A.; Kumar, S.; Joshi, N. Wide-angle X-ray diffraction (WXRD). In *Microscopy Methods in Nanomaterials Characterization*. Elsevier 2017, pp. 313−337, DOI: 10.1016/B978-0-323-46141-2.00009-2

(51) Bagheri, S.; Ramimoghadam, D.; Mansouri, N.; Hamid, B. A. S. Electrocatalytic activity of immobilized Co(II) on porous graphene aerogels. *J. Chin. Chem. Soc.* **2016**, *63*, 590−595.

(52) Wang, K.; Wang, Y.; Wang, C.; Xia, Y. Graphene oxide assisted solvothermal synthesis of $LiMnPO_4$ nanoplates cathode materials for lithium ion batteries. *Electrochim. Acta* **2014**, *146*, 8−14.

(53) Kim, J.; Cho, H.; Jeong, H. Y.; Ma, H.; Lee, J.; Hwang, J.; Park, M.; Cho, J. Self-induced concentration gradient in nickel-rich cathodes by sacrificial polymeric bead clusters for high-energy lithium-ion batteries. *Adv. Energy Mater.* **2017**, 1602559.

(54) Gao, W.; Mueller, J. E.; Anton, J.; Jiang, Q.; Jacob, T. Nickel cluster growth on defect sites of graphene: a computational study. *Angew. Chem., Int. Ed.* **2013**, *52*, 14237−14241.

(55) Ambrusi, R. E.; Orazi, V.; Marchetti, J. M.; Pronsato, M. E. Ni clusters embedded in multivacancy graphene substrates. *J. Phys. Chem. Solids* **2020**, *138*, No. 109258.

(56) Koutavarapu, R.; Cho, M.; Shim, J.; Rao, M. C. Structural and electrochemical properties of $LiNiO_2$ Cathodes prepared by solid state reaction method. *Ionics* **2020**, *26*, 5991−6002.

(57) Kosova, N. V.; Devyatkina, E. T.; Kaichev, V. V. Optimization of Ni^{2+}/Ni^{3+} ratio in layered $Li(Ni,Mn,Co)o_2$ cathodes for better electrochemistry. *J. Power Sources* **2007**, *174*, 965−969.

(58) Kalyani, P.; Kalaiselvi, N. Various aspects of $LiNiO_2$ chemistry: a review. *Sci. Technol. Adv. Mater.* **2005**, 689−703.

(59) Ryu, T.; Haldorai, Y.; Rengaraj, A.; Shin, J.; Hong, H. J.; Lee, G. W.; Han, Y. K.; Huh, Y. S.; Chung, K. S. Recovery of lithium ions from seawater using a continuous flow adsorption column packed with granulated chitosan-lithium manganese oxide. *Ind. Eng. Chem. Res.* **2016**, *55*, 7218−7225.

(60) Sun, Y.; Wan, P.; Pan, J.; Xu, C.; Liu, X. Low temperature synthesis of layered $LiNiO_2$ cathode material in air atmosphere by ion exchange reaction. *Solid State Ionics* **2006**, *177*, 1173−1177.

(61) Aziz, M.; Halim, F. S. A.; Jaafar, J. Preparation and characterization of graphene membrane electrode assembly. *J. Teknol.* **2014**, *69*, 11−14.

(62) Tian, X. H.; Zhou, Y. K.; Wu, G.; Wang, P. C.; Chen, J. Controllable synthesis of porous $LiFePO_4$ for tunable electrochemical Li-insertion performance. *Electrochim. Acta* **2017**, *229*, 316−324.

(63) Mao, G.; Xiao, F.; Zeng, L.; Tang, R.; Li, J.; Zhou, Q.; Wang, Y. Improvement of cycle performance of the high nickel cathode material $LiNi_{0.88}Co_{0.07}Al_{0.05}O_2$ for lithium-ion batteries by the spray drying of V_2O_5. *J. Alloys Compd.* **2022**, *892*, No. 162161.

(64) Zhu, Y.; Huang, Y.; Du, R.; Tang, M.; Wang, B.; Zhang, J. Effect of Ni^{2+} on lithium-ion diffusion in layered $LiNi_{1−x−y}Mn_xCo_yO_2$ materials. *Crystals* **2021**, *11*, 465.

(65) Fu, Z.; Hu, J.; Hu, W.; Yang, S.; Luo, Y. Quantitative analysis of Ni^{2+}/Ni^{3+} in $Li[Ni_xMn_yCo_z]O_2$ cathode materials: non-linear least-squares fitting of XPS spectra. *Appl. Surf. Sci.* **2018**, *441*, 1048−1056.

(66) Park, C. W.; Lee, J. H.; Seo, J. K.; Jo, W. Y.; Whang, D.; Hwang, S. M.; Kim, Y. J. Graphene collage on Ni-rich layered oxide cathodes for advanced lithium-ion batteries. *Nat. Commun.* **2021**, *12*, 1−10.

(67) Basirun, W. J.; Saeed, I. M.; Rahman, M. S.; Mazari, S. A. Nickel oxides/hydroxides-graphene as hybrid supercapattery nanocomposites for advanced charge storage materials − a review. *Crit. Rev. Solid State Mater. Sci.* **2021**, *46*, 553−586.

(68) Liu, D.; Wang, F.; Wang, G.; Lv, C.; Wang, Z.; Duan, X.; Li, X. Well-wrapped Li-rich layered cathodes by reduced graphene oxide towards high-performance Li-ion batteries. *Molecules* **2019**, *24*, 1680.

(69) Zhang, X.; Belharouak, I.; Li, L.; Lei, Y.; Elam, J. W.; Nie, A.; Chen, X.; Yassar, R. S.; Axelbaum, R. L. Structural and electro-chemical study of Al_2O_3 and TiO_2 coated $Li_{1.2}Ni_{0.13}Mn_{0.54}Co_{0.13}O_2$ cathode material using ALD. *Adv. Energy Mater.* **2013**, *3*, 1299−1307.

(70) Jabeen, M.; Ishaq, M.; Song, W.; Xu, L.; Deng, Q. Synthesis of Ni/Co/Al-layered triple Hydroxide@Brominated Graphene hybrid on nickel foam as electrode material for high-performance super-capacitor. *RSC Adv.* **2017**, *7*, 46553−46565.

(71) Shuai, H.; Jun, W.; Yao, L.; Lishan, Y.; Lijun, X.; Shuangshuang, Z.; Lixiong, B.; Chenghuan, H.; Chunxian, Z.; Jian, Z.; Wen-Yi, Z.; Youyuan, Z.; Yahui, Y. An epitaxial coating with preferred orientation stabilizing high-energy Ni-rich NCA cathodes. *Appl. Surf. Sci.* **2022**, *579*, No. 152183.

(72) Chen, T.; Li, X.; Wang, H.; Yan, X.; Wang, L.; Deng, B.; Ge, W.; Qu, M. The effect of gradient boracic polyanion-doping on structure, morphology, and cycling performance of Ni-Rich $LiNi_{0.8}Co_{0.15}Al_{0.05}O_2$ Cathode *Material. J. Power Sources* **2018**, *374*, 1−11.

(73) Li, J.; Wang, L.; Zhang, Q.; He, X. Synthesis and characterization of $LiNi_{0.6}Mn_{0.4-X}Co_xO_2$ as cathode materials for li-ion batteries. *J. Power Sources* **2009**, *189*, 28−33.

(74) Yue, P.; Wang, Z.; Peng, W.; Li, L.; Guo, H.; Li, X.; Hu, Q.; Zhang, Y. Preparation and electrochemical properties of submicron $LiNi_{0.6}Co_{0.2}Mn_{0.2}O_2$ as cathode material for lithium ion batteries. *Scr. Mater.* **2011**, *65*, 1077−1080.

(75) Hou, P. Y.; Zhang, L. Q.; Gao, X. P. A High-energy, full concentration-gradient cathode material with excellent cycle and thermal stability for lithium ion batteries. *J. Mater. Chem. A* **2014**, *2*, 17130−17138.

(76) Park, T. J.; Lim, J. B.; Son, J. T. Effect of calcination temperature of size controlled microstructure of $LiNi_{0.8}Co_{0.15}Al_{0.05}O_2$ cathode for rechargeable lithium battery. *Bull. Korean Chem. Soc.* **2014**, *35*, 357−364.

(77) Ravikumar, B.; Mynam, M.; Rai, B. Effect of salt concentration on properties of lithium ion battery electrolytes: a molecular dynamics study. *J. Phys. Chem. C* **2018**, *122*, 8173−8181.

(78) Pee, J. H.; Kim, Y. J.; Kim, C. Y.; Cho, W. S.; Kim, H. T. Direct synthesis of large scale AlN sheet. *Mater. Sci. Eng.* **2013**, 47.

(79) Teichert, P.; Eshetu, G. G.; Jahnke, H.; Figgemeier, E. Degradation and aging routes of Ni-rich cathode based Li-ion batteries. *Batteries* **2020**, 6.

(80) Lei, J.; McLarnon, F.; Kostecki, R. In situ Raman microscopy of individual $LiNi_{0.8}Co_{0.15}Al_{0.05}O_2$ particles in a Li-ion battery composite cathode. *J. Phys. Chem. B* **2005**, *109*, 952−957.